CORA Cork Open Research Archive
Cartlann Taighde Oscailte Chorcaí

Title	Galaxy size and rotation curve diversity in ΛCDM with baryons
Authors	Cruz, Akaxia;Brooks, Alyson M.;Lisanti, Mariangela;Peter, Annika H.G.;Geda, Robel;Quinn, Thomas;Tremmel, Michael;Munshi, Ferah;Keller, Ben;Wadsley, James
Publication date	2026-07-10
Original Citation	Cruz, A, Brooks, A M, Lisanti, M, Peter, A H G, Geda, R, Quinn, T, Tremmel, M, Munshi, F, Keller, B & Wadsley, J 2026, 'Galaxy size and rotation curve diversity in ΛCDM with baryons', Astrophysical Journal, vol. 1005, no. 2, 157, pp. 1-24. https://doi.org/10.3847/1538-4357/ae69ce
Type of publication	Article (peer-reviewed)
Link to publisher's version	10.3847/1538-4357/ae69ce
Rights	© 2026. The Author(s). Published by the American Astronomical Society. Original content from this work may be used under the terms of the https://creativecommons.org/licenses/by/4.0/. Any further distribution of this work must maintain attribution to the author(s) and the title of the work, journal citation and DOI. - https://creativecommons.org/licenses/by/4.0/
Download date	2026-11-02 20:15:23
Item downloaded from	https://hdl.handle.net/10468/19013

UCC
University College Cork, Ireland
Coláiste na hOllscoile Corcaigh

The Astrophysical Journal, 1005:157 (24pp), 2026 July 10 https://doi.org/10.3847/1538-4357/ae69ce
© 2026. The Author(s). Published by the American Astronomical Society.
OPEN ACCESS

Galaxy Size and Rotation Curve Diversity in ΛCDM with Baryons

Akaxia Cruz[1,2,3,13], Alyson M. Brooks[1,4], Mariangela Lisanti[1,2], Annika H. G. Peter[5,6,7], Robel Geda[3], Thomas Quinn[8], Michael Tremmel[9], Ferah Munshi[10], Ben Keller[11], and James Wadsley[12]
[1] Center for Computational Astrophysics, Flatiron Institute, New York, NY 10010, USA
[2] Department of Physics, Princeton University, Princeton, NJ 08544, USA
[3] Department of Astrophysical Sciences, Princeton University, Princeton, NJ 08544, USA
[4] Department of Physics & Astronomy, Rutgers, The State University of New Jersey, Piscataway, NJ 08854, USA
[5] Department of Physics, Ohio State University, Columbus, OH 43210, USA
[6] Department of Astronomy, Ohio State University, Columbus, OH 43210, USA
[7] Center for Cosmology and AstroParticle Physics (CCAPP), The Ohio State University, Columbus, OH 43210, USA
[8] Department of Astronomy, University of Washington, Seattle, WA 98195, USA
[9] School of Physics, University College Cork, T12 K8AF, Ireland
[10] Department of Physics & Astronomy, George Mason University, Fairfax, VA 22030, USA
[11] Department of Physics and Material Science, The University of Memphis, Memphis, TN 38152, USA
[12] Department of Physics and Astronomy, McMaster University, Ontario, L8S 4L8, Canada
Received 2025 October 8; revised 2026 April 27; accepted 2026 May 5; published 2026 July 2

Abstract

The observed rotation curves of dwarf galaxies exhibit significant diversity at fixed halo mass, challenging galaxy formation within the cold dark matter (CDM) model. Previous cosmological galaxy formation simulations with baryonic physics fail to reproduce the full diversity of rotation curves, suggesting that there is a flaw in baryonic feedback models, observational bias, or that an alternative to CDM must be invoked. In this work, we use the Marvelous Massive Dwarf zoom-in simulations, a suite of high-resolution dwarf simulations with $M_{200} \sim 10^{10}$–10^{11} $M_\odot$and $M_* \sim 10^7$–10^9 $M_\odot$, designed to target the mass range where the galaxy rotation curve diversity is maximized, i.e., between $V_{\rm max} \sim 70$ and 100 km s^{-1}. We add to this a set of low-mass galaxies from the Marvel Dwarf Zoom Volumes to extend the galaxy mass range to lower values. Our fiducial star formation and feedback models produce simulated dwarfs with a broader range of rotation curve shapes, similar to observations. These simulations both create dark matter cores via baryonic feedback, reproducing the slower-rising rotation curves, while also allowing for compact galaxies and steeply rising rotation curves. Our simulated dwarfs also reproduce the observed size–M_* relation, including scatter, producing both extended and compact dwarfs for the first time in simulated field dwarfs. However, the slowly rising and high baryon mass fraction, as well as the steeply rising and low baryon mass fraction, remain missing. We explore star formation and feedback models and conclude that previous simulations may have had feedback that was too strong to produce compact dwarfs.

Unified Astronomy Thesaurus concepts: Cold dark matter (265); Dark matter density (354); Galaxy formation (595); Dwarf galaxies (416); Hydrodynamical simulations (767); Stellar feedback (1602)

1. Introduction

Observations showing that rotation curves (RCs) are flat at large radii provided some of the first evidence for more matter in galaxies than can be accounted for by gas and stars (V. C. Rubin et al. 1980; A. Bosma 1981). Since then, it has been determined that dark matter comprises ∼85% of all matter in the Universe (Planck Collaboration et al. 2020). The cold dark matter (CDM) model describes the Universe well on large scales (e.g., V. Springel et al. 2006), but has encountered trouble explaining the diversity of RC shapes, particularly in dwarf galaxies (L. V. Sales et al. 2022). Dark-matter-only (DMO) simulations show universal, self-similar halo density profiles (Navarro–Frenk–White or NFW profiles; J. F. Navarro et al. 1996, 1997) that are steeper than some inferred from the RCs of dwarf galaxies (R. A. Flores & J. R. Primack 1994; B. Moore 1994; W. J. G. de Blok et al. 2001; W. J. G. de Blok 2010; S.-H. Oh et al. 2011). Hydrodynamic simulations have shown that the inclusion of energetic feedback from baryons can fluctuate the gravitational potential at the centers of dwarf galaxies, transforming an initially steep density profile into a more shallow profile, thought to reconcile simulations with slowly rising RCs (J. I. Read & G. Gilmore 2005; S. Mashchenko et al. 2008; F. Governato et al. 2012; A. Pontzen & F. Governato 2012; R. Teyssier et al. 2013; A. Di Cintio et al. 2014a; J. I. Read et al. 2016a; E. Tollet et al. 2016; A. Benítez-Llambay et al. 2019; A. A. Dutton et al. 2019).

However, it has more recently been recognized that the full range of RCs—from quickly to slowly rising—has not been fully reproduced by galaxy simulations (K. A. Oman et al. 2015; I. M. Santos-Santos et al. 2018; I. M. E. Santos-Santos et al. 2020; R. A. Jackson et al. 2025). In particular, K. A. Oman et al. (2015) highlight the diversity of observed RCs, showing that the diversity is maximized at $V_{\rm max}$ (the maximum observed RC velocity) ∼70–80 km s^{-1}, with a factor of ∼ 4 spread within the central 2 kpc ($V_{\rm 2kpc}$) at this fixed $V_{\rm max}$. A similar central velocity spread relative to $V_{\rm max}$ is found in Spitzer Photometry and Accurate RCs (SPARC; F. Lelli et al. 2016a), as well as more recent Hα RCs (N. C. Relatores et al. 2019a, 2019b).

[13] Corresponding author.

Original content from this work may be used under the terms of the Creative Commons Attribution 4.0 licence. Any further distribution of this work must maintain attribution to the author(s) and the title of the work, journal citation and DOI.

Previous simulations with CDM and baryons have struggled to reproduce the full range of the observed diversity of RCs. In particular, K. A. Oman et al. (2015) found a lack of diversity in the Evolution and Assembly of GaLaxies and their Environments (EAGLE; R. A. Crain et al. 2015; J. Schaye et al. 2015) simulations, though they explicitly used simulations that do not transform dark matter cusps into cores. I. M. Santos-Santos et al. (2018) examined the diversity in the Numerical Investigation of a Hundred Astrophysical Objects (NIHAO; L. Wang et al. 2015) simulations, which do create dark matter cores (e.g., A. Di Cintio et al. 2014a, 2014b). They demonstrated that using the gravitational midplane potential to calculate RCs better modeled dwarf galaxies that were out of dynamical equilibrium due to bursty feedback, as opposed to using shells of enclosed mass that assume spherical symmetry. No matter the RC calculation method, the NIHAO simulations fail to capture the RCs that rise more quickly than predicted by NFW (see also M. Frosst et al. 2022). Likewise, I. M. E. Santos-Santos et al. (2020) showed that EAGLE-CHT10 simulations with a high density threshold for star formation (the gas density above which stars form) can produce cored dark matter profiles with slowing rising RCs, but struggle to simultaneously produce the most quickly rising RCs. R. A. Jackson et al. (2025) used the NewHorizon simulations (Y. Dubois et al. 2021) with a high density threshold for star formation, finding they could also form cored dark matter profiles with slowly rising RCs at redshift $z = 0.2$. While they could also produce quickly rising RCs, they lacked a population of slowly rising RCs in galaxies with low baryonic contributions, at odds with the observations.

In contrast, simulations with lower density thresholds for star formation are able to produce the more quickly rising RCs, but not the more slowly rising ones. Similarly, F. A. Roper et al. (2023) showed a correspondence between a high (low) star formation density threshold and slowly (quickly) rising RCs. Further, F. A. Roper et al. (2023) showed that simulations that do not create dark matter cores can produce a broader range of observed diversity, due to the noncircular motions present in the simulations and observed in mock H I (neutral atomic hydrogen) RCs.

SPARC suggests an additional observed diversity in the galaxy size–stellar mass plane. Observations show the presence of both compact and extended galaxies at a given stellar mass (M_*). Previous hydrodynamical simulations within CDM struggle not only to produce the diversity in RCs, but also the diversity in the size–M_* plane (L. V. Sales et al. 2022). F. Jiang et al. (2019) showed that NIHAO, Feedback in Realistic Environments 2 (FIRE-2; P. F. Hopkins et al. 2018), and the simulations presented in A. Lupi et al. (2017) produce galaxies that are more diffuse than the observed galaxies and struggle to produce the most compact galaxies at and below $M_* \sim 10^9\ M_\odot$.

In this work, we use high-resolution hydrodynamical cosmological simulations of dwarf galaxies produced using the Charm *N*body Gravity solver (ChaNGa) code with multiple feedback models to examine the diversity of RCs and galaxy sizes compared to observations. We show that a new suite of dwarf galaxies—the Marvelous Massive Dwarf zooms—produce a range of both quickly and slowly rising RCs at a given halo mass when run with our fiducial model. In addition, the galaxies also produce a more realistic range of sizes at stellar masses $M_* \sim 10^7$–$10^9\ M_\odot$, consistent with the scatter showing both extended and compact galaxies in observations.

This paper is organized as follows. In Section 2, we detail the galaxy formation models used in our simulated sample. In Section 3, we briefly describe the observational data with which we compare our simulated results. We detail our analysis techniques used throughout this work in Section 4. We present our RC diversity shapes in Section 5.1 and explore the impact of baryons on RC shapes in Section 5.2. In Section 5.3, we then discuss the diversity in the size–M_* plane, and in Section 6, we consider how subgrid physics can prevent the formation of compact galaxies. We discuss how our results compare to previous works in CDM with baryons and in alternative dark matter models in Section 7, and finally we summarize our results in Section 8. In Appendix A, we detail how the method used to obtain RCs influences their shapes. In Appendix B, we briefly discuss feedback differences on RC shape. In Appendix C, we detail our density profiles and fitting procedure and show RC shape trends with the dark matter density slope.

2. Simulations

In this study, we use two suites of simulated dwarf galaxies: one collection of "zoom volumes" and a complementary set of more-massive individual zoom-in galaxy simulations. Both suites are produced using the *N*-body+Smooth Particle Hydrodynamics (SPH) code ChaNGa (H. Menon et al. 2015), which adopts hydrodynamic physics from Gasoline2 (J. W. Wadsley et al. 2004, 2017), but modified to use the charm++ runtime code for load balancing and communication. All simulations are run in a fully cosmological context. We run with a fiducial model on which most of the results are based, but we also rerun two galaxies with varying subgrid physics in Section 6. First, we detail the physics in common between the two simulation suites, then discuss their differences in Sections 2.1 and 2.2. In Section 2.3, we describe the additional variations used for the tests in Section 6. The final sample selection compared to the SPARC data (F. Lelli et al. 2016a; see Section 3) is defined in Section 4.

The fiducial star formation model for both simulation suites utilizes the metal-line-cooling and star formation scheme as presented in C. Christensen et al. (2012). This model includes the nonequilibrium formation and destruction of H_2 and a uniform time-dependent UV field (F. Haardt & P. Madau 2012) to model photoionization and heating. Lyman–Werner radiation from young stars is additionally tracked and can further heat and photodissociate H_2 and suppress star formation, mimicking early stellar feedback. Star particles represent stellar populations with a P. Kroupa (2001) initial mass function. The star particle initial mass is 30% of the original gas particle mass. Mass and metals from stars are returned to surrounding gas particles in winds and in type I and type II supernovae (SNe; G. Stinson et al. 2006).

Star formation is restricted to occur stochastically in the presence of H_2 when gas particles become cold ($T_* \leqslant 10^3$ K) and dense ($n_* \geqslant 0.1$ cm^{-3}). The probability of creating a star particle (with mass $m_{\rm star}$) from a gas particle (with mass $m_{\rm gas}$) with local dynamical time, $t_{\rm dyn}$, in time $\Delta t = 10^6$ yr is

$$p = \frac{m_{\rm gas}}{m_{\rm star}}\left(1 - {\rm e}^{-c_* X_{H_2} \Delta t / t_{\rm dyn}}\right), \quad (1)$$

where the value adopted for the star formation efficiency is $c_* = 0.1$. The star formation efficiency, c_*, times the fraction

of nonionized molecular hydrogen, X_{H_2}, produces the appropriate normalization of the Kennicutt–Schmidt relation (C. R. Christensen et al. 2014). Although the density threshold is low compared to other bursty star formation prescriptions (e.g., F. Governato et al. 2010; A. Benítez-Llambay et al. 2019; A. A. Dutton et al. 2019, 2020), the actual density of the star-forming gas tends to be closer to 100 cm^{-3}, due to the additional requirement that H_2 be present.

All of the simulations in our zoom-volume and fiducial zoom-in models include black hole (BH) formation and growth, with BH accretion and feedback models from M. Tremmel et al. (2015) and M. Tremmel et al. (2017). We do not make assumptions about BH halo occupation fractions. Instead, the BH seed formation is related to the physical state of the gas (i.e., temperature, density, metallicity, and molecular fraction) at high redshift.

The BHs are subject to a prescription of dynamical friction that follows the orbital evolution of BHs, as introduced by M. Tremmel et al. (2015). Correctly accounting for this effect can lead to pairs of supermassive BHs at kiloparsec-scale separations that survive for several Gyr (M. Tremmel et al. 2018). The BHs in our simulation also obey a modified Bondi accretion (M. Tremmel et al. 2017). The parameters for seeding and accretion are detailed for each simulation suite below.

Here, we have described the physics that the simulations have in common. Below, we describe the differences between the two suites. In summary, they use slightly different cosmologies and resolutions, they have slightly different seeding mechanisms for BHs, and their feedback implementations (for SNe II and BHs) are different. Despite that, previous works have used both sets of simulations simultaneously to increase the mass range of the simulated sample size. They were unable to find differences in the galaxy properties between the two runs—e.g., in stellar-to-halo mass, H I content and gas fractions, sizes, or metallicity (see D. R. Piacitelli et al. 2025; D. Ruan et al. 2025). We again combine them in this work to increase the range of galaxy masses and explore potential differences (see Appendix B.)

2.1. Marvel Dwarf Zoom Volumes

The Marvel dwarf suite (hereafter Marvel) consists of a population of dwarfs from "zoom volumes" (J. M. Bellovary et al. 2019; F. Munshi et al. 2021; C. R. Christensen et al. 2024). In contrast to typical zoom simulations that focus their Lagrangian regions on individual halos, in these simulations the Lagrangian regions are larger volumes that contain dozens of dwarf galaxies. The volumes for the Marvel zooms are selected to be between ∼1.5 and 7 Mpc away from Milky Way–mass galaxies (C. R. Christensen et al. 2024). These volumes represent isolated local-volume galaxies. Four such simulations are run, named CptMarvel, Elektra, Rogue, and Storm, with a WMAP3 cosmology ($\Omega_\Lambda = 0.736$, $\Omega_m = 0.264$, $\Omega_b = 0.0441$, $\sigma_8 = 0.805$, $n_s = 0.967$, and $h = 0.712$; D. N. Spergel et al. 2007). Each zoom volume has a spline force softening of $\epsilon = 60$ pc, an initial gas mass resolution of 1410 $M_\odot$, an initial stellar mass resolution of 420 $M_\odot$, and a dark matter mass resolution of 6650 $M_\odot$.

The Marvel simulations include a model for stellar feedback from SNe II, which adopts a "blastwave" implementation, as detailed in G. Stinson et al. (2006). This model deposits mass, thermal energy, and metals into nearby gas when a massive star of 8–40 $M_\odot$ becomes an SN. Each SN releases 1.5×10^{51} erg of energy into 32 neighboring gas particles, and a star particle deposits 1.5×10^{49} erg $M_\odot^{-1}$ over the lifetime of an SN II. After each SN, gas cooling is turned off for a time determined by Equation (11) in G. Stinson et al. (2006), the timescale over which the gas particle does not radiatively cool. The deposited energy, combined with the turning off of the cooling, is used to mimic how inefficient cooling influences the local interstellar medium (ISM). The Storm zoom volume is additionally run with superbubble feedback, which is introduced in the next subsection.

BH seeds form in the early Universe if the gas particle has already met the star formation threshold. Additionally, BH particles form in extremely dense ($n > 1.5 \times 10^4$ cm^{-3}) and cool ($T < 2 \times 10^4$ K) gas regions. To prevent fragmentation into stars, gas particles that can form BHs must also have a low metallicity ($Z < 10^{-4}$) and have a low molecular fraction ($X_{H_2} < 10^{-4}$). The mass of a BH seed is 5×10^4 $M_\odot$. BHs accrete according to a modified Bondi–Hoyle accretion, which accounts for the rotational support of the surrounding gas (M. Tremmel et al. 2017). The energy of the accretion onto the BHs is isotropically transferred to nearby gas particles as thermal energy, using the blastwave feedback model of G. Stinson et al. (2006) for the Marvel zoom volumes. However, J. M. Bellovary et al. (2019) found that the BHs in Marvel zoom volumes barely grow after their formation and thus impart very little energy.

2.2. The Marvelous Massive and Extended Dwarf Zooms

We analyze the Marvelous Massive Dwarf zooms, a collection of 40 zoom-in simulations with $M_{200} \sim (0.1–2) \times 10^{11}$ $M_\odot$ and stellar masses $M_* \sim (0.06–3) \times 10^9$ $M_\odot$, as well as the Extended Marvelous Dwarf zooms, which have stellar masses down to $M_* \sim 6 \times 10^6$ $M_\odot$. As suggested by the name, the Marvelous Massive Dwarfs are designed to have higher masses than the Marvel set. They are specifically run to investigate the mass range where the diversity of RCs is maximized and are selected based on their stellar mass, aiming for 10^8–10^9 $M_\odot$. Both the Marvelous Massive and Extended Marvelous dwarf zooms are selected from the $(25\ \mathrm{Mpc})^3$ box, Romulus25 (M. Tremmel et al. 2017). We choose halos that are at least 1.5 Mpc away from any galaxy with $M_* > 10^{10}$ $M_\odot$ at redshift $z = 0.1$. At a fixed stellar mass, they are chosen to span a range in halo mass. No other selection criteria are used. Since they are run with the same physics, we refer to the Marvelous Massive Dwarf zooms and the Extended Marvelous Dwarf zooms collectively as the Marvelous Massive Dwarf zooms or just the Massive Dwarfs, to not confuse results with previous work using the Marvel zoom-volume galaxies.

These 55 simulations are run at "Mint" resolution, with spline force softening of $\epsilon = 87$ pc, an initial gas mass resolution of 3300 $M_\odot$, an initial stellar mass resolution of 990 $M_\odot$, and a dark matter mass resolution of 1.8×10^4 $M_\odot$. All of our Marvelous Massive Dwarf zooms are run with a Planck Cosmology ($\Omega_\Lambda = 0.6914$, $\Omega_m = 0.3086$, $\Omega_b = 0.04825$, $\sigma_8 = 0.8288$, $n_s = 0.9611$, and $h = 0.6777$; Planck Collaboration et al. 2014) and use the "zoom-in" methods described by A. Pontzen et al. (2008).

We run the 40 Marvelous Massive Dwarf zooms and the 15 Extended Marvelous Dwarf zooms with a fiducial model that includes H_2 cooling, star formation, and superbubble feedback.

Stars preferentially form in clusters (S. Pfalzner et al. 2012; M. G. H. Krause et al. 2020). Feedback from clustered stars produces superbubbles, which are distinct from isolated SNe, as modeled by the blastwave model. The superbubble feedback model used here (B. W. Keller et al. 2014) introduces a multiphase treatment of gas, evaporation, and thermal conduction. Unlike the blastwave model, this feedback model does not explicitly shut off cooling. Instead, the evaporation from thermal conduction is designed to regulate the amount of hot gas. As in B. W. Keller et al. (2014), a star particle deposits 10^{49} erg $M_{\odot}^{-1}$ of thermal energy due to SNe II. This model deposits feedback into resolution elements in a brief multiphase state: the particles have different specific energies, masses, and densities in the hot bubble phase and the cold ISM phase. Then, for each phase, separate cooling rates can be derived, using their respective densities and temperatures. Gas particles become single-phase again when the hot phase either cools or evaporates the cool phase.

BH particles form in gas particles with high density ($n > 1.5 \times 10^4$ cm^{-3}), cool temperature ($T < 5 \times 10^3$ K), low metallicity ($Z < 10^{-5}$), low molecular fraction ($X_{H_2} < 2 \times 10^{-3}$), and large Jeans mass ($M_J > 10^5\ M_{\odot}$). These criteria are motivated by J. H. Wise et al. (2019), J. A. Regan et al. (2020), and J. Regan (2023). The mass of a BH seed is $10^5\ M_{\odot}$. BHs have a density-boosted Bondi accretion motivated by C. M. Booth & J. Schaye (2009), where the boost density threshold is 100 cm^{-3}. The energy of the accretion onto the BHs is isotropically transferred to nearby gas particles as thermal energy, using the superbubble feedback model of B. W. Keller et al. (2014) for the Massive Dwarf zooms. J. M. Bellovary et al. (2019) found little accretion in the Marvel galaxies, and we explored a subset of the Massive Dwarf zoom galaxies run with and without BHs and found no preferential shift in their stellar sizes or masses.

We visually examine the morphology of 40 of the most-massive galaxies in the Massive Dwarf zooms, shown as the mock U, V, and I Johnston filter (UVI) images in Figure 1. The images are "face-on" in the x–y plane, so that the angular momentum of each galaxy is rotated into the z-direction, which is out of the page. The zooms are ordered by stellar mass, M_*, from top to bottom and left to right in a given row. The zoom-in name is annotated in the upper left of each subpanel. The details of how the M_{200} and angular momentum are calculated are described in Section 4.1. From visual inspection, it can be seen that the galaxies have diverse morphologies and sizes, as a given row represents roughly the same stellar mass, and there is a diversity in size. Elongated "bar-like" galaxies that look similar to, e.g., r555, r618, and r563 in the Massive Dwarf suite are observed and classified as IB(s)m galaxies in the de Vaucouleurs classification system. An observed example galaxy is NGC 4449.

Beyond these galaxies having diverse morphologies, the simulations also agree well with other observables. In forthcoming work, we will demonstrate the ability to produce stellar dwarf galaxy disks (R. Geda et al. 2026) with stellar masses down to $10^7\ M_{\odot}$, which have been observed (F. Lelli et al. 2016a), but have evaded previous simulations (K. El-Badry et al. 2018; J. A. Benavides et al. 2025; B. M. Celiz et al. 2025). Additionally, the ChaNGa models make galaxies that are in better agreement with the observed stellar age gradients in dwarfs (C. L. Riggs et al. 2024), have H I sizes and gas fractions that match observed galaxies (D. Ruan et al. 2025), match the mass–metallicity relation and the sSFR–mass trends, and reasonably reproduce dwarf circumgalactic medium column densities (D. R. Piacitelli et al. 2025). We have additionally made predictions for the turn down in the baryonic Tully–Fisher relationship (D. Ruan et al. 2025) and in stellar shapes (B. Keith et al. 2025), which can further test the ChaNGa models used in this work.

2.3. NIHAO Reruns

Because ChaNGa adopts hydrodynamic physics from Gasoline, the code used for the NIHAO simulations, we can rerun the initial conditions with some of the subgrid physics used in L. Wang et al. (2015). In Section 6, we rerun two of the Massive Dwarf zoom-in galaxies that have quiescent merger histories after a cosmic time of ∼2 Gyr to better understand the differences between the NIHAO results and our simulations. Starting from the Mint resolution, fiducial star formation, and superbubble feedback model, we make incremental changes, progressing toward the NIHAO model and resolution. In the NIHAO star formation model, gas is eligible to form stars once it has reached specified density and temperature thresholds, in agreement with the Kennicutt–Schmidt Law. In the model adopted in L. Wang et al. (2015), which we mimic here, stars form in cold ($T_* < 1.5 \times 10^4$ K) and dense ($n_* > 10.3$ cm^{-3}) gas. The NIHAO star formation model deviates from our fiducial model significantly, with stars forming in much less dense and much warmer gas.

NIHAO uses the blastwave SN feedback model of G. Stinson et al. (2006), with star particles releasing a total of 10^{49} erg $M_{\odot}^{-1}$ thermal energy, due to SNe II as well as early stellar feedback from massive stars (G. S. Stinson et al. 2013). To limit star formation to agree with the abundance-matching value at the Milky Way scale, the early feedback efficiency, $\epsilon_{\rm ESF} = 13\%$, of the total stellar flux, 2×10^{50} erg $M_{\odot}^{-1}$, is ejected into the surrounding gas over the 4 Myr between a star's formation and when SNe II begin to occur. For our runs, we adopt a slightly lower $\epsilon_{\rm ESF} = 10\%$, consistent with G. S. Stinson et al. (2013).

The NIHAO simulations are run with constant relative resolution between the gravitational softening of the dark matter $\epsilon_{\rm DM}$ and halo virial radius across ∼3 dex of halo mass and have ∼10^6 dark matter particles per halo. This means that each halo mass scale is run at a different resolution. We approach the mass resolution of the NIHAO runs for the $M_{200} \sim 10^{10}$–$10^{11}\ M_{\odot}$ halos[14] by stepping from our "Mint" resolution to "Near Mint," which has half the force resolution (174 pc) and 8 times lower mass resolution (initial gas particle masses of $2.64 \times 10^4\ M_{\odot}$ and dark matter mass resolution of $1.4 \times 10^5\ M_{\odot}$).

We change one subgrid physics prescription at a time, to isolate the impact on stellar half-light radius and mass. Independent of resolution, in all of the runs with NIHAO subgrid physics models, we exclude BHs, since the NIHAO runs we compare to do not include them (I. M. Santos-Santos et al. 2018). The details of these physics variations are discussed in Section 6.

[14] In NIHAO, $M_{200} = (2.63$–$7.12) \times 10^{10}\ M_{\odot}$ halos have a dark matter mass resolution of $6.426 \times 10^4\ M_{\odot}$, a baryon (gas and stars) mass resolution of $1.173 \times 10^4\ M_{\odot}$, and a gravitational softening of $\epsilon_{\rm gas} = 132.6$ pc for gas and $\epsilon_{\rm DM} = 310.5$ pc for dark matter.

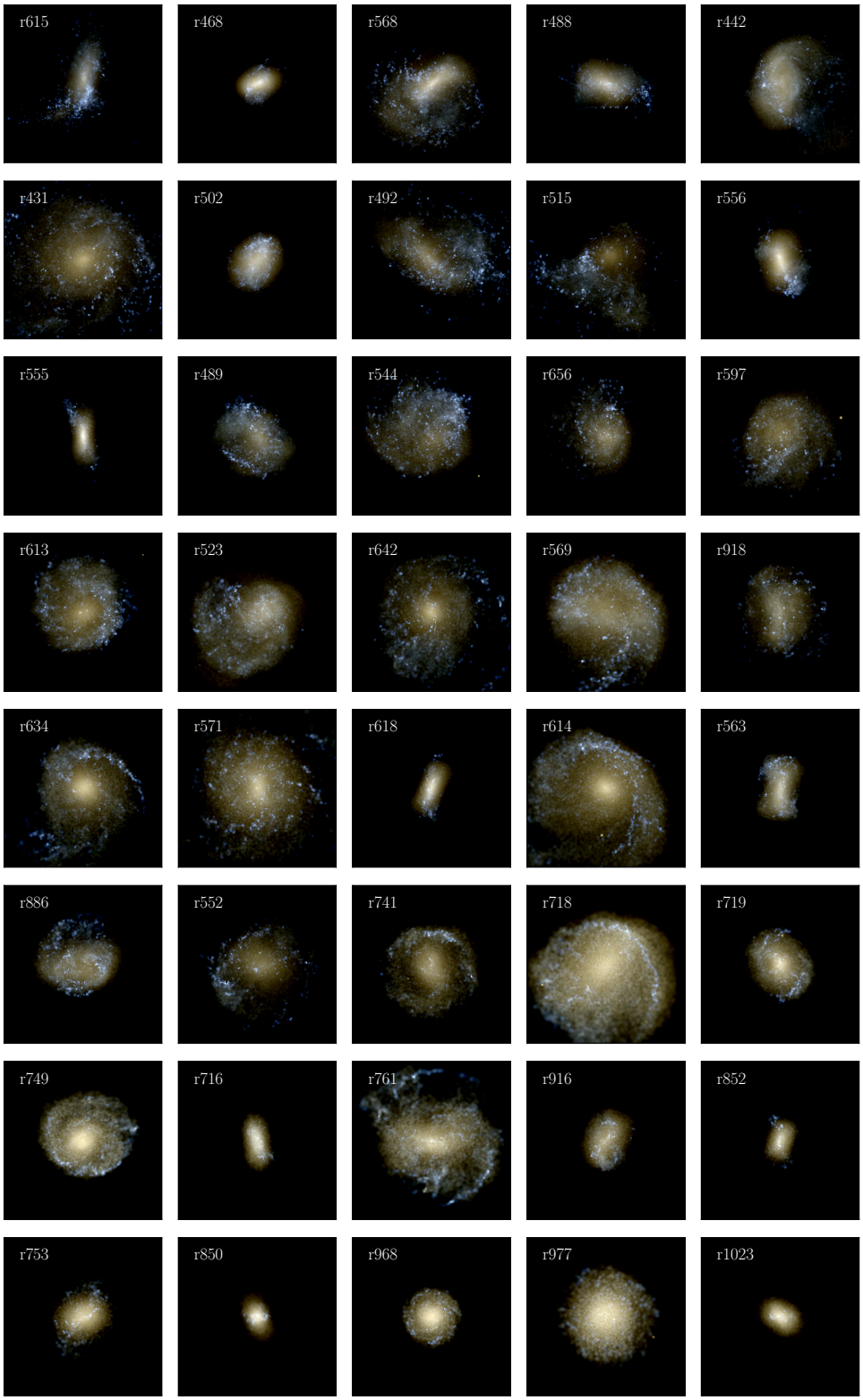


Figure 1. Mock UVI images of 40 of the Massive Dwarf zoom-in galaxies at $z = 0$, ordered by decreasing M_*, from top left to bottom right. The zoom-in name is annotated in the upper left of each subpanel. Each galaxy is shown face-on (i.e., with the angular momentum vector out of the page), and each square panel has a side length of 15 kpc. Visually, it is clear that the Massive Dwarf zooms have diverse morphologies.

3. Observational Data

We compare our numerical results to observed galaxies from the SPARC dataset (F. Lelli et al. 2016a). These observations comprise a sample of 175 nearby galaxies with homogeneous photometry at 3.6 μm, which complements high-quality RC data from previous H I and/or Hα observations. Since the velocity dispersion of H I is typically on the order of $\sim$10 km s^{-1}, we expect pressure support to be significant only in very low-mass dwarf galaxies with rotation

velocities of $\sim$20 km s^{-1} (F. Lelli et al. 2012). However, the reported SPARC RCs have been corrected for pressure support, beam smearing, and inclination. The stellar masses are derived by assuming a mass-to-light ratio of $M_*/L_{[3.6\,\mu m]} = 0.5$.

The sample of SPARC galaxies considered in this analysis only includes those with inclinations $i > 30°$, as in I. M. E. Santos-Santos et al. (2020), and those suitable for dynamical studies with a quality flag $Q \neq 3$, as in A. Zentner et al. (2022), to minimize RCs with substantial uncertainties. We use the RCs from F. Lelli et al. (2016a) to calculate the V_{max} values for the observed sample. We take the maximum value of the observed RCs out to the last observed radial bin to be V_{max} for the observed sample, noting that in some cases this value might underpredict the true maximum circular velocity. This is more common in the lower-mass galaxies, as the observational H I limit is still on the rising part of the RC (see, e.g., D. Ruan et al. 2025 for more details on how our simulated galaxies are impacted).

4. Analysis

4.1. Halo Finding and Centering

We identify halos in a given simulation using the AMIGA halo finder (AHF; S. R. Knollmann & A. Knebe 2009). The virial radius, R_{vir}, of a halo is the radius at which the density corresponds to $\Delta_h = 200$ times the critical density of the Universe, ρ_c. All halos in this work are analyzed at $z = 0$. We calculate the virial mass of halos as

$$M_{vir} = \frac{4\pi}{3} \Delta_h \rho_c R_{vir}^3 . \quad (2)$$

We center each halo using the shrinking-sphere procedure (C. Power et al. 2003) and Lorentz boost into the rest frame of the center of mass of the particles within 1 kpc of the center. We then rotate the galaxy in the x–y plane, such that the angular momentum vector of the gas within 5 kpc of the halo center points in the z-direction. We do produce disk galaxies and, in these systems, the z-component of the total angular momentum is well aligned with the z-direction (R. Geda et al. 2026). However, even for the nondisky galaxies, we use the same orientation methodology.

4.2. RCs

This subsection describes the variety of methods used to calculate the RC velocities from our simulations and how we compare them with observations. We calculate full RCs between $r \in [r_{conv}, 15\,\mathrm{kpc}]$ using 100 linearly spaced bins. Below the convergence radius, r_{conv}, two-body scattering can alter the mass distribution (C. Power et al. 2003). A. D. Ludlow et al. (2019a) note that the convergence radius interior to which we expect artificial heating can be conveniently approximated as $r_{conv} = 0.055 \times l$, where $l = L_{box}/N_{part}^{1/3}$ is the mean interparticle spacing in physical units for a simulation with box length L_{box} and N_{part} total particles. In the Massive zooms, $r_{conv} \sim 0.45$ kpc, and in the Marvel simulations, $r_{conv} \sim 0.34$ kpc. The upper end of the considered radial range is motivated by the radius that corresponds to the true maximum halo velocity: we find $R_{max} < 15$ kpc for all systems considered in this work. The binning scheme is chosen so that each bin contains at least 3000 dark matter particles, even for the smallest-mass systems. In the higher-mass systems, each bin contains well over 3000 particles. The limit on particles per bin is expected to properly resolve densities (C. Power et al. 2003).

We calculate the RCs using two different methods, and then use two separate proxies to determine the maximum and central values. First, we assume spherical symmetry and calculate

$$V^{circ}(r) = \sqrt{\frac{GM(<r)}{r}} , \quad (3)$$

where G is Newton's constant, and $M(<r)$ is the total enclosed mass at the galactocentric radius r. The total enclosed mass within a sphere of specified radius is determined using PYNBODY (A. Pontzen et al. 2013). The second approach is to use the velocity derived from the gravitational potential, $\Phi(R)$, in the midplane of the galaxy as

$$V^{mid}(R) = \sqrt{R\frac{\partial\Phi(R)}{\partial R}}\Bigg|_{z=0} , \quad (4)$$

where R is the cylindrical radius, and $z = 0$ denotes the x–y plane, as discussed in Section 4.1. This calculation is also done using PYNBODY.

We determine the maximum velocity of a given RC in two ways. The first is to take the maximum of the total simulated RC. In this case, we define the maximum velocities for RCs using spherical symmetry and the midplane potential as V_{max}^{circ} and V_{max}^{mid}, respectively. The second is to instead use the maximum velocity for HI-limited RCs within a radius, R_1, that is consistent with observational limits. Observed low-mass dwarfs have RCs that are sometimes still rising at the detection limit in their last radial bin (B. Catinella et al. 2006; R. Kuzio de Naray et al. 2006), implying that the true maximum of their RCs may not be measured (L. V. Sales et al. 2017; D. Ruan et al. 2025). To align our simulation results with observational limits, we calculate the H I gas mass surface density in cylindrical shells from the host center. We define R_1, the 2D projected size of the H I disk, as the radius where $\Sigma_{HI} = 1\,M_\odot\,\mathrm{pc}^{-2}$, as motivated by, e.g., A. H. Broeils & M. H. Rhee (1997) and J. Wang et al. (2016). Again, we find $R_1 < 15$ kpc for all systems considered in this work. We define the maximum velocities for HI-limited RCs using spherical symmetry and the midplane potential as $V_{max}^{circ+HI}$ and V_{max}^{mid+HI}, respectively.

Once the maximum velocity V_{max} (V_{max}^{circ} or $V_{max}^{circ+HI}$ for spherical symmetry or V_{max}^{mid} or V_{max}^{mid+HI} for the midplane potential) is determined, a proxy for the central rotation velocity is taken to be

$$V_{fid} = V_{rot}(r = r_{fid}) , \quad (5)$$

where $r_{fid}/\mathrm{kpc} = V_{max}/(35\,\mathrm{km\,s^{-1}})$ is motivated by I. M. E. Santos-Santos et al. (2020). V_{rot} is the RC obtained using any of the four methods described above (e.g., circ, circ +HI, mid, or mid+HI), which we also indicate in the superscript to V_{fid}. V_{fid} is chosen as the proxy for the central velocity, so we can consistently explore the RC diversity and compare with previous works (I. M. E. Santos-Santos et al. 2020; E. R. Downing & K. A. Oman 2023; F. A. Roper et al. 2023). While K. A. Oman et al. (2015) used 2 kpc, r_{fid} carries the benefit of probing the central parts of an RC, independent of halo mass. V_{fid} is selected so that simulations and most high-resolution H I observations of dwarfs are able to resolve this

radius, allowing for comparison between the two. We explicitly explore the differences between the definitions of the maximum and fiducial velocities in Section 5.1.

For the observed RCs from F. Lelli et al. (2016a), we calculate $V_{\rm fid}$ using the same method as for the simulated curves. In particular, the maximum velocity, $V_{\rm max}$, is determined for each galaxy in the SPARC sample identified in Section 3 out to the last observed radial bin. Then, for each SPARC RC, we calculate $r_{\rm fid}$ and take $V_{\rm fid}$ to be the rotational velocity in the radial bin closest to that radius.

We limit our analysis to the simulated and observed dwarf galaxies with stellar masses in the range $M_* \sim (5 \times 10^6)$–$(1 \times 10^9)\,M_\odot$. We restrict the SPARC sample to galaxies with $V_{\rm max} < 100$ km s^{-1}, since that is the range for most of the simulated galaxies.[15] By including resolved galaxies outside the virial radius of the main host, we can increase the Massive Dwarf set by seven more galaxies. This results in 47 galaxies from the Marvelous Massive Dwarf zoom suite, 15 galaxies from the Extended Marvelous Massive Dwarf zooms, and 23 from the Marvel suite, for a total of 85 simulated galaxies.

The Massive Dwarf zoom-in simulations include quickly and slowly rising RCs consistent with observations, as demonstrated in Figure 2. In particular, we show examples of four SPARC RCs that exhibit different behavior at a roughly fixed $V_{\rm max} \sim 80$–90 km s^{-1}. In each panel, we also show the RCs' $V^{\rm mid}$ (solid lines) and $V^{\rm circ}$ (dashed lines) for a selected simulation. HI-limited RCs ($V^{\rm mid+HI}$ and $V^{\rm circ+HI}$) are plotted in black, whereas RCs beyond R_1 are shown in dark gray, suggesting that the RC would not be detected in resolved H I observations at these large radii. In the lowest-mass systems ($V_{\rm max} \lesssim 60$ km s^{-1}), the true $V_{\rm max}$ can exist at $R_{\rm max} > R_{\rm l}$ (see, e.g., D. Ruan et al. 2025 and the right panel of Figure A1 for examples of such systems). Further, the fiducial radius, $r_{\rm fid}$, can also be greater than R_1. In these cases, the ratio $\eta_{\rm rot} = V_{\rm fid}/V_{\rm max}$, a proxy for how fast or slow the RCs rise in the central region, may be larger than the true value if the RC is still rising.

In Figure 2, the RCs derived using the midplane potential peak at larger velocities and at larger radii than the mass-enclosed case, specifically for the systems with disks (r492 and r569). This general shift is consistent with the analytic prediction for RCs of the same mass enclosed in a disk compared to those distributed spherically (J. Binney & S. Tremaine 2008). Since $r_{\rm fid}$ scales with $V_{\rm max}$ (Equation (5)), this shift also implies a shift in $V_{\rm fid}$. The full RCs from SPARC (F. Lelli et al. 2016a) are plotted in dark teal. The observed diversity contrasts of an NFW RC with $V_{\rm max} \sim 87$ km s^{-1} are shown in gray, with the shaded band representing the scatter in the mass–concentration relation from A. D. Ludlow et al. (2016). The NFW $V_{\rm max}$ is selected to be intermediate to those of the observed RCs. The self-similar NFW halo density profile is parameterized by the dark matter halo mass (J. F. Navarro et al. 1996, 1997) and thus predicts identical RCs for fixed $V_{\rm max}$, which is a proxy for the mass of the system. A gray dotted line corresponding to the NFW RCs' $r_{\rm fid}$ is plotted to demonstrate how $V_{\rm fid}$ represents a central RC velocity. The SPARC RCs in the upper-left and lower-right panels of Figure 2 are more quickly rising than the NFW prediction, with $V_{\rm max} = 86.6$ km s^{-1}, but have lower $V_{\rm max} = 82.6$ km s^{-1} and $V_{\rm max} = 84.3$ km s^{-1}, respectively. The most slowly rising SPARC RC in the upper-right panel instead has a very similar $V_{\rm max} = 86.9$ km s^{-1}. The SPARC RC with the shape closest to NFW has a $V_{\rm max}$ that is 0.9 km s^{-1} lower than the NFW RC.

[15] One simulated galaxy with $V_{\rm max} > 100$ km s^{-1} at $z = 0$ has $V_{\rm max} < 100$ km s^{-1} at $z = 0.1$, after which it underwent a major merger.

4.3. Galaxy Sizes

To determine the galaxy sizes, we use PYNBODY to measure the half-light radius of its stars, $r_{1/2}$, in the Johnson K band, using cylindrical coordinates. The K band is used to mimic SPARC (F. Lelli et al. 2016a). PYNBODY computes the magnitudes of star particles in the K band using the Padova simple stellar populations (P. Marigo et al. 2008), converts magnitudes to luminosities for all star particles, constructs a galaxy's total luminosity profile, and identifies the radius that encloses half of that luminosity. To verify our effective radii measurements, we generate mock K-band images of all our galaxies using PYNBODY and measure their Petrosian profiles ($\eta(r)$; V. Petrosian 1976) with circular apertures using PETROFIT (R. Geda et al. 2022). The Petrosian radius ($r_{\rm p}$) is defined as the radius at which the profile reaches a predefined Petrosian index ($\eta_{\rm p}$, where $\eta(r_{\rm p}) = \eta_{\rm p}$). The total flux radius is then calculated by multiplying the Petrosian radius by a constant ($r_{\rm total} = \epsilon_{\rm p} \cdot r_{\rm p}$). Measurements using Sloan Digital Sky Survey parameters ($\eta_p = 0.2$ and $\epsilon_{\rm p} = 2$; M. A. Strauss et al. 2002) yield nearly identical values between Petrosian half-light radii (i.e., $L(\leqslant r_{0.5}) = 0.5L(\leqslant r_{\rm total})$, where L is the projected luminosity) and our PYNBODY-derived effective radii. Furthermore, for galaxies whose light profiles are well described by a single-component Sérsic model (J. L. Sérsic 1963), we fit 2D Sérsic profiles using PETROFIT. The effective radii parameters of the fitted single-component Sérsic models are within 0.3 kpc of our effective radii measurements.

5. Diversity of RCs

5.1. RC Shapes

We quantify the diversity of the simulated RC shapes by comparing the fiducial velocities, $V_{\rm fid}$, to the maximum circular velocities, $V_{\rm max}$, in Figure 3. RCs derived with a spherical enclosed mass (Equation (3)) are plotted in the top row, and those using the midplane calculation (Equation (4)) are plotted in the bottom row. The left column takes the maximum of the RCs out to R_1, while the right column uses the maximum of the total simulated RC. In each panel, the SPARC data points are shown as gray diamonds, the Marvel galaxies are the teal squares, and the Massive Dwarf zooms are the purple circles. The 1: 1 line is shown in dashed black, and the NFW prediction is shown by the gray shaded region. For a given $V_{\rm max}$, the associated NFW RC is obtained by sampling the concentration from the A. D. Ludlow et al. (2016) relation; the bands in the figure correspond to the rms scatter from the concentration uncertainty. For an NFW RC with a given $V_{\rm max}$, the associated $r_{\rm fid}$ is derived, then the $V_{\rm fid}$ is calculated using Equation (5). We denote low-mass objects that do not have sufficient H I outside the resolved region ($r_{\rm conv}$) with black outlines. These objects are not shown in the cases where $V_{\rm max}$ is determined out to R_1 (left column).

To start, we compare the different RC methods against each other, starting with the circ and mid methods. For the case of circ and circ+HI (top row), most simulated galaxy RCs have a $V_{\rm fid}$ that is above or in agreement with the NFW prediction at a given $V_{\rm max}$. The mid and mid+HI cases (bottom row) both

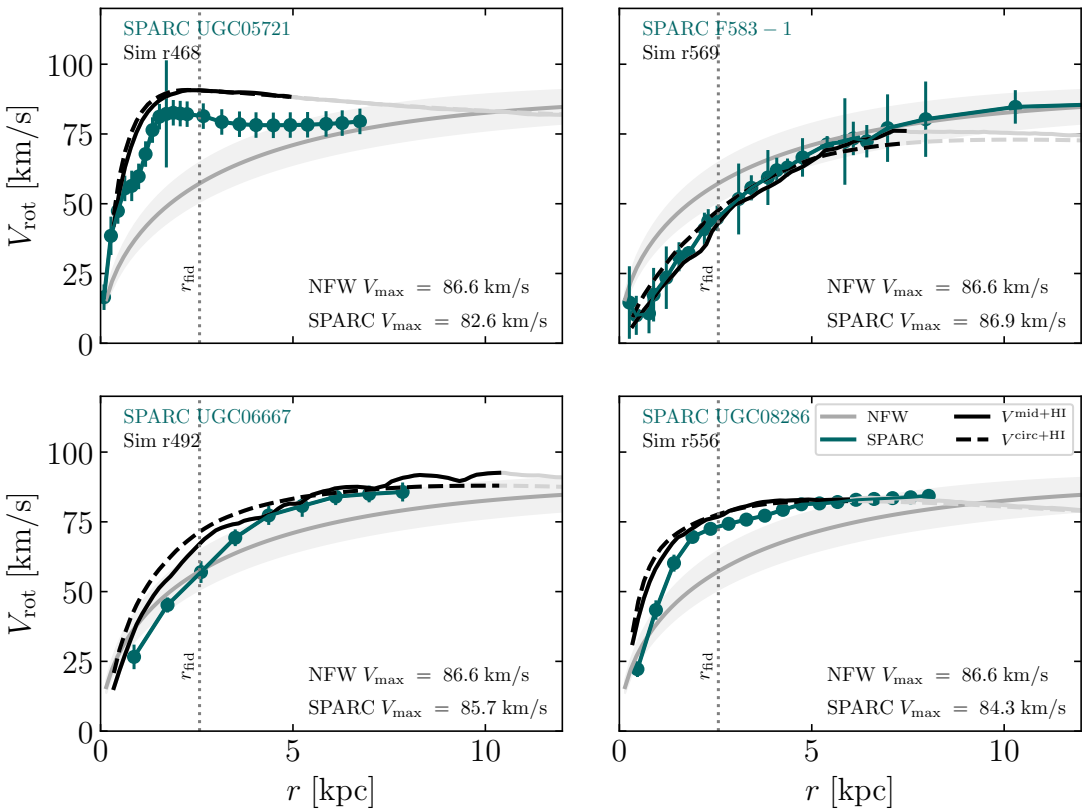


Figure 2. RCs for sample galaxies from SPARC with $V_{max} \sim 80$–90 km s^{-1}. The full SPARC RCs are shown in dark teal. In each panel, a simulated Massive Dwarf RC with similar shape and V_{max} to the SPARC RC is shown using spherical symmetry (Equation (3)) with a dashed line and from the midplane potential (Equation (4)) with a solid line. The full simulated RCs are shown for both cases with dark gray lines (V^{circ} and V^{mid}), and the HI-limited RCs are shown in black ($V^{circ+HI}$ and V^{mid+HI}). An NFW RC with $V_{max} \sim 87$ km s^{-1}, intermediate to the observed RCs, is shown with scatter in the NFW mass–concentration relationship by the light-gray shaded region. The dotted gray line is the fiducial radius r_{fid} associated with the NFW RCs. For the two simulations with disks (r492 and r569), the rotation speeds from the midplane potential peak higher and at larger radii than the RCs from the mass-enclosed method. Both the midplane and mass-enclosed RCs exhibit diversity that mimics the observed RCs; the RCs in the upper-left and lower-right panels are more quickly rising than the NFW case. In contrast, the upper right is more slowly rising, and the lower left is in rough agreement with the NFW RC.

exhibit a lower median and more extended spread in V_{fid}, for given V_{max}, than seen in the top row. For example, for halos with $V_{max} = 60$–80 km s^{-1}, the absolute 16th–50th–84th percentiles for V_{fid} are $56.3^{61.8}_{48.1}$ km s^{-1} and $45.2^{56.7}_{34.1}$ km s^{-1} for circ+HI and mid+HI, respectively.

In Appendix A, we examine the shifts for individual galaxies when changing from circ+HI to mid+HI and from circ to mid. The left panel of Figure A1 shows the shift between the upper and lower right panels of Figure 3. For the more-massive galaxies, i.e., with $V_{max} \gtrsim 60$ km s^{-1}, the largest shifts occur for systems with disks (see Appendix A for the disk definition). These galaxies both shift to higher V_{max} and also lower V_{fid}. As mentioned above, a disk potential causes the RC to peak at larger velocities and at larger radii than a spherical potential (J. Binney & S. Tremaine 2008). Changing from the circ to mid method naturally captures the change in potential in disk-dominated galaxies. At lower V_{max}, shifts can occur in systems without disks. Previous works have shown that low-mass galaxies have bursty star formation with feedback that drives the galaxies out of equilibrium (e.g., J. I. Read et al. 2016a; K. El-Badry et al. 2017; R. Verbeke et al. 2017; E. R. Downing & K. A. Oman 2023; I. S. Sands et al. 2026). If galaxies are undergoing outflows from the midplane, this will reduce the measurement using the midplane potential relative to the mass enclosed in spherical shells. Since outflows are centralized (e.g., C. B. Brook et al. 2011), this will be more likely to reduce V_{fid} than V_{max}, consistent with the shifts seen in the lower-mass galaxies in Figure A1. In summary, while the specific mechanism that causes the shift differs across V_{max}, in both cases the shift is due to the deviation from spherical symmetry.

Next, we examine the shifts in RC shape due to measuring V_{max} within R_1 instead of using the full V_{max} determined from the simulations. In the HI-limited case (the left panels of Figure 3), there are a number of systems where $V_{max} \sim V_{fid}$, falling close to the 1: 1 line. These same galaxies do not lie near the 1: 1 line when measuring the full V_{max}, instead agreeing well with the NFW prediction. The right panel of Figure A1 examines this shift, which occurs predominantly in low-V_{max} galaxies. In such low-mass systems, the full RCs are still rising at R_1. RCs that are still rising in the last HI-limited radial bin are also observed (e.g., K. B. W. McQuinn et al. 2022), and indeed similar objects exist in the SPARC sample. In these systems, by definition V_{max} is measured at a smaller radius in the HI-limited case than in the full case, resulting in lower V_{max}. Because r_{fid} is determined by V_{max}, V_{fid} is also measured at a smaller radius. Figure A1 shows that the shift tends to be larger in V_{max} than in V_{fid}, but the overall effect is that V_{max} and V_{fid} are measured much closer together in radius, and the overall galaxy shifts toward the 1: 1 line.

Throughout the rest of the work, we use the mid+HI method, because we expect it to most closely mimic mock observations—i.e., capturing the impacts of disk potentials,

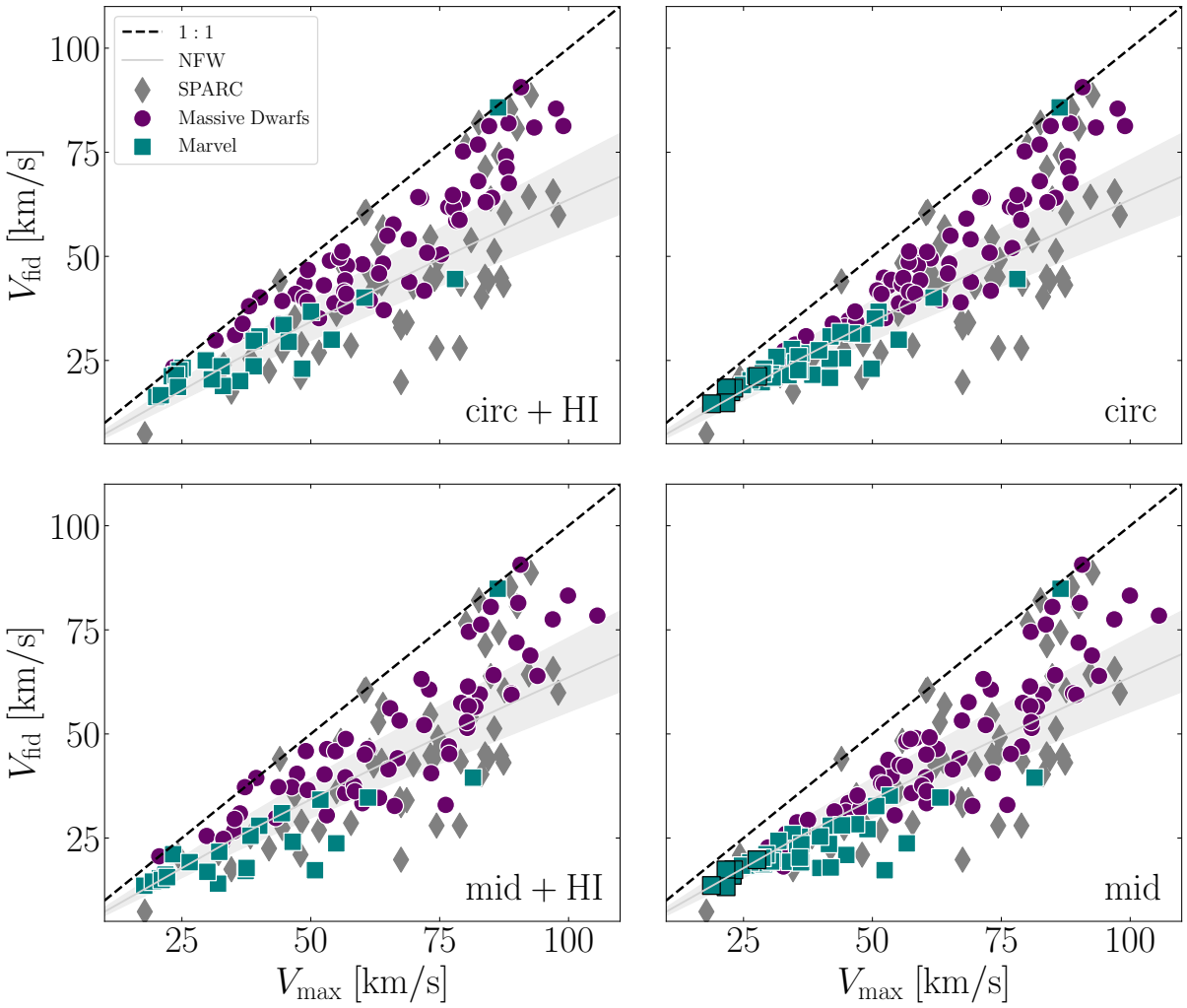


Figure 3. The fiducial velocity versus maximum circular velocity for SPARC is shown in gray diamonds, the Massive Dwarf zooms in purple circles, and the Marvel dwarfs in teal squares. The NFW prediction is shown by the gray line, with the shaded region representing the rms scatter in the mass–concentration relation reported in A. D. Ludlow et al. (2016). The dashed black 1: 1 line represents where $V_{\rm fid}$ is equal to $V_{\rm max}$. The results correspond to the following velocities: $V^{\rm circ+HI}$ (upper left), $V^{\rm circ}$ (upper right), $V^{\rm mid+HI}$ (lower left), and $V^{\rm mid}$ (lower right). For some of the lowest-mass Marvel galaxies, there is limited H I and $R_1 < r_{\rm conv}$; we mark these galaxies with black outlines on the teal squares, to denote that they are HI-limited and excluded from the left panels. A larger spread in inner velocities at $r_{\rm fid}$ at fixed $V_{\rm max}$ is predicted for the midplane potential compared to the spherical case. RCs that are more quickly and more slowly rising than NFW are predicted with the midplane method down to $V_{\rm max}^{\rm mid+HI} \sim 50$ km s^{-1} in the Massive Dwarf zooms.

dynamical disequilibrium, and the observational R_1 limit. Hence, it is likely the method that best mimics the SPARC data. However, there are many other effects that can change the observed RCs of galaxies that will not be captured by any of the measurement methods, including mid+HI. We refer the reader to Section 7.1 for a more in-depth discussion.

When the mid+HI method is used, we find a broad range of diversity in the $V_{\rm fid} - V_{\rm max}$ plane, with galaxies that rise both more slowly and more quickly than NFW. To quantify the spread in $V_{\rm fid}$, we split the SPARC and simulation samples into four evenly spaced $V_{\rm max}$ bins between 20 and 100 km s^{-1} and quantify the median $V_{\rm fid}$ and 16th–84th percentiles in each. The results are summarized in Table 1. We note that this method is not perfect, as each sample has a different selection function (for the simulation suites, the selection criteria are discussed in Section 2), but it aids in comparing the samples. This table helps us explore how well either simulation set matches the observational SPARC data and whether the two simulation sets produce consistent predictions for RC shape at fixed $V_{\rm max}$. Note that we do not comment on bins that are statistically limited, with fewer than five galaxies in them.

In the upper $V_{\rm max} = 80$–100 km s^{-1} bin, the median and upper percentiles for SPARC and the Massive Dwarf zooms agree well; however, the lower percentile for SPARC is $\sim$10 km s^{-1} smaller. This is visually evident in Figure 3, as we do not reproduce a few of the most slowly rising objects in SPARC between $V_{\rm max} \sim 80$and 100 km s^{-1}. While the simulations do not directly reproduce these types of observed RCs, if they are subject to similar out-of-equilibrium gas processes as found in other simulations, including full mock-observational effects might allow them to reach the observed parameter space of slowly rising RCs (F. A. Roper et al. 2023). This is discussed in further detail in Section 7.1.

In the $V_{\rm max} = 60$–80 km s^{-1} bin, the Massive Dwarf zooms agree very well with SPARC. In particular, SPARC has $V_{\rm fid} = 44.1^{54.5}_{33.0}$, while the mid+HI case has a slightly higher median but a similar percentile range, with $V_{\rm fid}^{\rm mid+HI} = 45.2^{56.7}_{34.1}$ km s^{-1}. The Marvel zoom volumes only have a single object in this $V_{\rm max}$ range, so we cannot derive statistical results.

Table 1
Binned RC Shape Statistics for SPARC and Simulated Galaxies

V_{max} (km s^{-1})	SPARC V_{fid} (km s^{-1})	Massive Dwarfs V_{fid}^{mid+HI} (km s^{-1})	Marvel V_{fid}^{mid+HI} (km s^{-1})
20–40	$21.4^{24.4}_{19.6}$ (5)	$28.1^{36.5}_{24.9}$ (8)	$17.1^{22.0}_{15.3}$ (13)
40–60	$28.8^{40.6}_{24.4}$ (10)	$37.4^{45.9}_{36.0}$ (16)	$24.1^{32.1}_{21.4}$ (5)
60–80	$44.1^{54.5}_{33.0}$ (20)	$45.2^{56.7}_{34.1}$ (17)	34.7 (1)
80–100	$63.9^{80.9}_{44.7}$ (19)	$64.1^{80.6}_{56.7}$ (19)	$62.2^{77.6}_{46.8}$ (2)

Note. V_{fid} statistics are derived for four evenly spaced V_{max} bins between 20 and 100 km s^{-1}. In each column, the absolute 16th–50th–84th percentiles are provided for the specified sample, with the number of galaxies in that bin indicated in parentheses. For the simulated galaxies, V_{max}^{mid+HI} and V_{fid}^{mid+HI} values are reported. The Massive Dwarfs and SPARC have similar 16th–50th–84th percentiles between $V_{max} = 60$ and 80 km s^{-1} and similar 50th–84th percentiles between $V_{max} = 80$ and 100 km s^{-1}, but the Massive Dwarfs have a higher 16th percentile in this range, indicating the more slowly rising RCs are missing in this bin. In the two lowest-V_{max} bins, neither simulation suite independently matches the SPARC data well.

In the two lowest-V_{max} bins, neither simulation suite independently matches the SPARC data well. The Massive Dwarf zooms have higher medians than SPARC, with the lower quartile not encompassing the SPARC median. The Marvel zoom volumes have lower medians compared to SPARC, but the upper quartile does a better job of encompassing the median SPARC V_{fid} values.

The differences between the two simulation suites could arise from their different feedback prescriptions. The Massive Dwarf zooms are run with superbubble feedback, whereas the Marvel zoom volumes are run with blastwave feedback. In Figure B1 of Appendix B, we compare the diversity of RCs for galaxies in the Marvel Storm zoom volume, run with both blastwave and superbubble feedback, using V^{mid+HI}. There is a preference toward larger V_{max}^{mid+HI} for a given galaxy in the runs with superbubble feedback. B. Azartash-Namin et al. (2024) compared galaxy and halo properties in superbubble versus blastwave feedback. They found no change in stellar size between the two feedback models, but they did find that the simulations with superbubble feedback have preferentially higher halo masses compared to their blastwave counterparts (see their Figure 1). We postulate that this preference for higher halo masses is translated into larger V_{max}^{mid+HI} in superbubble compared to blastwave feedback in the Storm simulations.

The impact of the higher V_{max}^{mid+HI} in the superbubble runs on the diversity of RCs is not immediately obvious. Most of the galaxies in Figure B1 move mostly along the NFW expectation when changing from blastwave to superbubble feedback. This is because V_{fid}^{mid+HI} tends to be slightly higher as well. However, the most-massive galaxy in that set makes it clear that an increase in V_{max} can introduce more diversity if V_{fid} remains approximately constant. At the moment, it is not conclusive whether the choice of feedback model impacts the diversity of RCs, or in what direction.

For a fixed V_{max} in the midplane case, we find values of V_{fid} both above and below the NFW prediction. This is in contrast to other simulation suites, such as NIHAO, which only show slowly rising RCs when using the midplane method in the V_{max} range considered in this work (I. M. Santos-Santos et al. 2018). Similarly, EAGLE-CHT10 simulations run with a high density threshold for star formation also struggled to produce the most quickly and the most slowly rising RCs (I. M. E. Santos-Santos et al. 2020). In both the NIHAO and EAGLE-CHT10 simulations that preferentially made slowly rising RCs, baryonic feedback also induced dark matter density cores in the central galaxy. In Appendix C, we show that the Marvel and Massive Dwarf simulations can produce cored dark matter density profiles—i.e., these simulations simultaneously make dark matter cores while also producing quickly rising RCs. In the next section, we explore the relation between the baryonic distribution and the RCs in these new simulations.

5.2. The Influence of Baryons on the Diversity of RCs

How baryons contribute to RC shapes, and whether the shapes of RCs are correlated with baryonic surface densities, are debated questions. T. Ren et al. (2019) showed that the shape of SPARC RCs correlates with surface brightness, at least for galaxies in their highest-V_{max} bin, 79–91 km s^{-1}. However, I. M. E. Santos-Santos et al. (2020) demonstrated that dwarf galaxies show a broad range in RC shape at a given baryonic surface density, concluding that the RC shape and surface brightness are not correlated, in contrast to T. Ren et al. (2019). In this subsection, we investigate the relation between the baryonic distribution and RC shape in the Marvel and Massive Dwarf galaxy suites.

To quantify the connection between the RC shape and baryonic distribution in our simulations, we define baryonic surface densities using the baryonic half-mass radius. Following Section 4.3, we calculate the cumulative luminosity profile for the stars and then convert to mass using a mass-to-light ratio of $\Upsilon_* = M_*/L_* = 0.5\, M_\odot\, L_\odot^{-1}$ (S. S. McGaugh & J. M. Schombert 2014; F. Lelli et al. 2016a, 2016b). The value of $\Upsilon_* \approx 0.5\, M_\odot\, L_\odot^{-1}$ was found to minimize the scatter around the baryonic Tully–Fisher relationship (F. Lelli et al. 2016b) and to be consistent with stellar population synthesis models with standard initial mass functions (S. S. McGaugh & J. M. Schombert 2014). The mass profiles are calculated this way, instead of taking the stellar mass directly from the simulations to mimic the observational procedure. The enclosed H I gas mass profile is calculated out to R_1 and multiplied by 1.4 to account for helium and metals in the gas phase (D. Arnett 1996; J. D. Bradford et al. 2016). Consistent with F. Lelli et al. (2016a), we do not account for the contribution of molecular gas, because such data are not available for most SPARC galaxies and molecules are expected to be subdominant compared to stars and atomic gas (J. D. Simon et al. 2003; B. S. Frank et al. 2016). We find that $R_1 > r_{1/2}$, in agreement with SPARC (F. Lelli et al. 2016a). The simulated stellar and gas enclosed mass profiles are added, and we find the radius $r_{1/2,bar}$, where half of the total baryonic mass, $M_{bar} = M_* + 1.4M_{HI}$, is enclosed. Then, we calculate the baryonic surface density as $\Sigma_{bar} = M_{bar}/2\pi r_{1/2,bar}^2$, consistent with I. M. E. Santos-Santos et al. (2020).

To calculate the baryonic surface densities for SPARC galaxies, we derive gravitational baryonic contributions to the RCs, $V_{bar}^2(r) = V_{gas}^2(r) + \Upsilon_* V_*^2(r)$, from published mass models (F. Lelli et al. 2016a). We note that for the SPARC galaxies considered in this study, there are no stellar bulge contributions to V_*. The baryonic half-mass radii are derived using spherical symmetry with $M_{bar}(<r) = rV_{bar}^2(r)/G$.

To probe the connection between the baryonic surface density and RC shape, the left panel of Figure 4 examines the set of galaxies with $V_{max}^{mid+HI} = 79$–91 km s^{-1}, to match

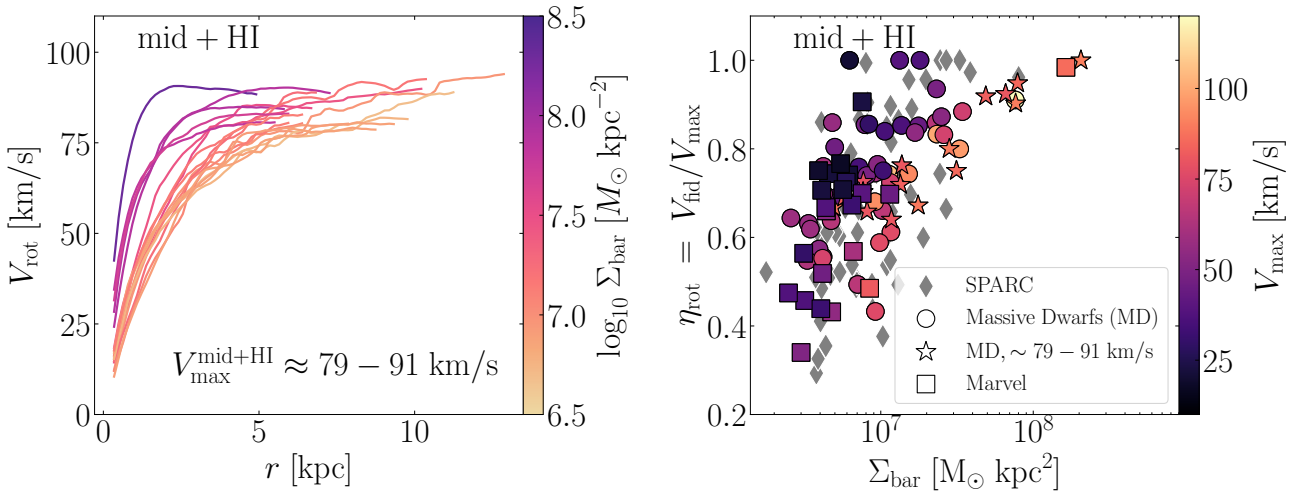


Figure 4. Left: midplane RCs colored by baryonic surface density. The RCs are cut off at R_1 and are chosen in a $V_{\rm max}$ range that matches with T. Ren et al. (2019). The HI-limited midplane method is used to calculate $V_{\rm fid}$ and $V_{\rm max}$. The most quickly rising RCs (violet) have higher surface densities, whereas the more slowly rotating RCs (orange) have lower surface densities. This trend is consistent with the observed RCs in the same $V_{\rm max}$ range (F. Lelli et al. 2016a). Right: $\eta_{\rm rot}$ versus $\Sigma_{\rm bar}$, with the simulated galaxies colored by $V_{\rm max}$ and the SPARC data in gray. In the simulated and observed galaxies, higher-mass systems have higher baryonic surface densities and have RCs that tend to rise more quickly. There is large scatter in $\eta_{\rm rot}$ at lower $\Sigma_{\rm bar}$. Systems with $V_{\rm max} \sim 79$–91 km s^{-1} that appear in the left panel are highlighted with star markers.

T. Ren et al. (2019).[16] The R_1 cut causes each RC to end at a different radius, as for the observed galaxies. For this range of $V_{\rm max}^{\rm mid+HI}$, the most quickly rising RCs have high baryonic surface densities; baryons dominate the central potentials in these systems (see, for example, the density profiles for r488, r502, r468, and r555 in Figure C1). On the other hand, the more slowly rising RCs have low baryonic surface densities. However, this trend does not exist for lower $V_{\rm max}$ values than those shown here, in agreement with I. M. E. Santos-Santos et al. (2020).

The parameter

$$\eta_{\rm rot} = V_{\rm fid}/V_{\rm max} \tag{6}$$

is a proxy for the shape of an RC, as it compares the central velocity with its maximum (I. M. E. Santos-Santos et al. 2020). For the NFW model, $\eta_{\rm rot}$ increases slightly with decreasing $V_{\rm max}$. As a benchmark, note that galaxies with $\eta_{\rm rot} \gtrsim 0.65$–$0.75$ are more quickly rising in their central regions than the corresponding NFW prediction (with scatter from the mass–concentration relation), and galaxies with $\eta_{\rm rot} \lesssim 0.55$ are more slowly rising. The right panel of Figure 4 shows the relationship between $\eta_{\rm rot}$, the baryonic surface density $\Sigma_{\rm bar}$, and $V_{\rm max}^{\rm HI+mid}$ for the full simulated and observed samples. The galaxies shown in the left panel are indicated as stars, making it obvious that there is a clear trend between $\eta_{\rm rot}$ and baryonic surface density for galaxies with $V_{\rm max}^{\rm mid+HI} = 79$–$91$ km s^{-1}. In the simulations, galaxies with a higher baryonic surface density tend to be more quickly rising—i.e., have larger $\eta_{\rm rot}$ values. However, there is significant scatter for galaxies with $\Sigma_{\rm bar} < 10^7\ M_\odot$ kpc^{-2}, showing that the correlation with baryonic surface density evident in the left panel does not hold at lower $V_{\rm max}$ values.

The simulated galaxies with the most quickly rising RCs (i.e., those with high $\eta_{\rm rot}$) bracket the range of surface densities in the observations, although the (two) highest-mass simulated galaxies have higher surface densities than SPARC. On the other hand, at every $\Sigma_{\rm bar} < 3 \times 10^7\ M_\odot$ kpc^2, there is a subset of SPARC galaxies that are more slowly rising than the simulations. These SPARC systems may be influenced by noncircular motions (J. I. Read et al. 2016b; E. R. Downing & K. A. Oman 2023) or inclination (F. A. Roper et al. 2023), making them appear more slowly rising. We discuss these effects further in Section 7.1.

In addition to surface densities, we examine the relationship between the central baryonic mass fraction and RC shape using mass models for the SPARC data (F. Lelli et al. 2016a). Assuming spherical symmetry, the central baryonic mass fraction within $r_{\rm fid}$ can be quantified using RCs with

$$\eta_{\rm bar} \equiv (V_{\rm b,fid}/V_{\rm fid})^2\ , \tag{7}$$

where $V_{\rm b,fid}$ is the fiducial velocity of the baryonic RCs. I. M. E. Santos-Santos et al. (2020) used this definition and $\eta_{\rm rot}$ to explore how the central baryon mass fraction relates to the shapes of RCs, as in Figure 5. The SPARC data are indicated by the diamonds in both panels, colored by $V_{\rm max}$ for the left and indicated in gray for the right. The NIHAO galaxies extracted from I. M. E. Santos-Santos et al. (2020) are shown in light blue on the left. The Massive Dwarf galaxies (circles) and Marvel dwarfs (squares) are colored by their $V_{\rm max}^{\rm mid+HI}$ on the right panel.

For galaxies with lower baryonic mass fractions ($\eta_{\rm bar} \lesssim 0.5$), we find simulated galaxies with a spread in RC shape $\eta_{\rm rot}$ including objects that rise more quickly than the NFW prediction. This is in contrast to the NIHAO results shown in Figure 5—and also those for EAGLE-CHT10 (I. M. E. Santos-Santos et al. 2020), which are not shown. In particular, the observed dwarfs in the upper left of each panel in Figure 5, which are more quickly rising than NFW ($\eta_{\rm rot} \gtrsim 0.75$) and have low $\eta_{\rm bar}$, are absent in NIHAO. However, the Massive Dwarf zoom galaxies occupy this space. These simulated systems are influenced by the HI-limited velocity measurement method, pushing them closer the 1: 1

[16] We do not color by surface brightness, as in T. Ren et al. (2019), but the baryonic surface density and brightness should be consistent up to a scaling factor for a fixed mass-to-light ratio, as advocated for in F. Lelli et al. (2016a).

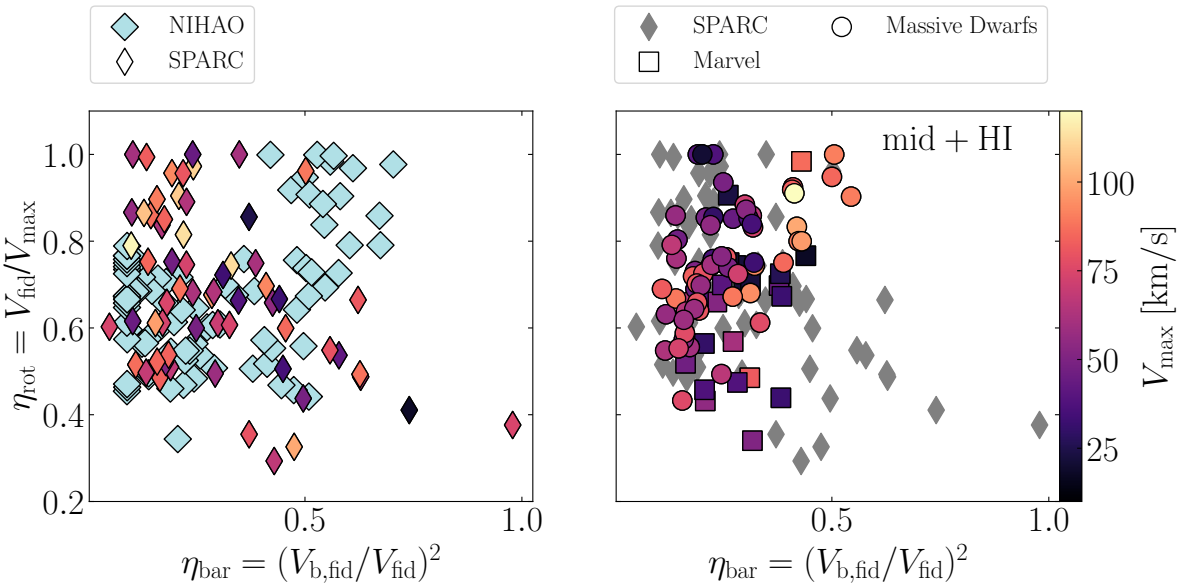


Figure 5. $\eta_{\rm rot}$ versus baryon mass fraction within $r_{\rm fid}$, colored by $V_{\rm max}$. Left: SPARC data, in thin colored diamonds, with mass modeling from F. Lelli et al. (2016a). The objects in the upper-left region have low central baryon mass fractions, but are still more quickly rising in their central regions than the NFW prediction. Previous CDM and baryon simulations have struggled to reproduce these objects. This is demonstrated for NIHAO data (from I. M. E. Santos-Santos et al. 2020) in the light blue diamonds, including galaxies with $V_{\rm max} > 100$ km s^{-1} and measured using enclosed mass with no R_1 limit (referred to as the "circ method" in this work). Right: the Massive Dwarf zooms are shown in circles, and the Marvel sample in squares, using the mid+HI method to calculate velocities. Most of the simulated galaxies have $\eta_{\rm bar} \lesssim 0.5$. There is a significant spread in $\eta_{\rm rot}$ in this region, including some systems with $\eta_{\rm rot} \gtrsim 0.75$, higher than the NFW prediction.

line, as discussed in Section 5.1 and shown in Appendix A (see Figure A2). Although there are simulated galaxies in the upper-left region, the higher $V_{\rm max}$ SPARC systems in this region are still missing from our sample.

R. A. Jackson et al. (2025) similarly found quickly rising RCs with low $\eta_{\rm bar}$ using lower-resolution simulated galaxies in NewHorizon, but again only in lower-mass systems and at a much earlier cosmic time than the SPARC galaxies. Instead, F. A. Roper et al. (2023) examined two simulated galaxies and showed that systems with high $\eta_{\rm rot}$ and low $\eta_{\rm bar}$ could be found in mock H I RCs along special viewing angles, an effect that we neglect here.

Other SPARC galaxies of interest have RCs that are slowly rising (low $\eta_{\rm rot}$), but have large central baryonic mass fractions (high $\eta_{\rm bar}$). These are the SPARC galaxies in the lower-right corner of the $\eta_{\rm rot} - \eta_{\rm bar}$ plane in Figure 5. They are the same SPARC objects that are missing from the Massive Dwarf and Marvel simulations below the NFW prediction in Figure 3 and the missing slowly rising objects in Figure 4. NIHAO, EAGLE-CHT10, and NewHorizon simulations that create dark matter cores do a better job of producing slowly rising objects with larger baryon mass fractions. However, even in NIHAO, a fraction of these SPARC systems are still missing, as shown in the left panel of Figure 5. Similarly, the most slowly rising systems are missing in R. A. Jackson et al. (2025). It is possible that all of the simulated galaxies, including those presented here, have mass-loading factors too high relative to real galaxies (e.g., M. L. M. Collins & J. I. Read 2022). Indeed, as we explore below, we believe the NIHAO simulations have stronger feedback than our fiducial runs, preventing them from making both the steeply rising galaxies and compact galaxies. Alternatively, I. M. Santos-Santos et al. (2018), F. A. Roper et al. (2023), and K. A. Oman et al. (2019) suggest that the observed galaxies in the lower-right corner may be affected by noncircular motion.

In this subsection, we have explored how and if baryons impact the diversity of RC shapes. Our simulations are able to produce quickly rising RCs with low central baryon mass fractions that other simulations producing cores have had difficulty producing. We think the reason is partially due to the inclusion of the R_1 cut on the RCs, used to mimic observations. Alternatively, $\eta_{\rm bar}$ may be biased by assuming spherical symmetry rather than accounting for a disk geometry. However, there is a subset of slowly rising SPARC galaxies that we do not reproduce, and we see this in a variety of different galaxy property planes. Moreover, these galaxies tend to have nonnegligible contributions of baryons. While these objects may be better produced for stronger feedback models, as in EAGLE-CHT10 and NIHAO (I. M. E. Santos-Santos et al. 2020), we suspect they may instead be influenced by noncircular motions, as suggested by I. M. Santos-Santos et al. (2018), K. A. Oman et al. (2019), and F. A. Roper et al. (2023), because the strong feedback scenario prevents the formation of the compact galaxies found in SPARC (e.g., F. Jiang et al. 2019). We examine the role of feedback in Section 6.

5.3. Diversity in the Size–M$_*$ Plane

Beyond the diversity in RCs, dwarf galaxies are observed to have a spread in size at a given M_* (S. G. Carlsten et al. 2021). In Section 5.2, we found that RCs exhibit a diversity of baryonic surface densities, which may be linked to the diversity of the size–M_* relationship. Figure 6 examines the relationship between $\eta_{\rm rot}$ versus $r_{1/2}$ for the Massive Dwarf and Marvel galaxies. Each simulated galaxy is colored by its stellar mass, M_*. Although there is scatter, objects with smaller $r_{1/2}$ tend to have higher $\eta_{\rm rot}$—i.e., simulated galaxies with quickly rising RCs (high $\eta_{\rm rot}$) are also the most compact. However, the converse is not true. Simulated galaxies with slowly rising RCs (low $\eta_{\rm rot}$) instead show a range of sizes. This is due to the size–M_* relationship and its scatter at a given mass. The relationship between $\eta_{\rm rot}$ and $r_{1/2}$

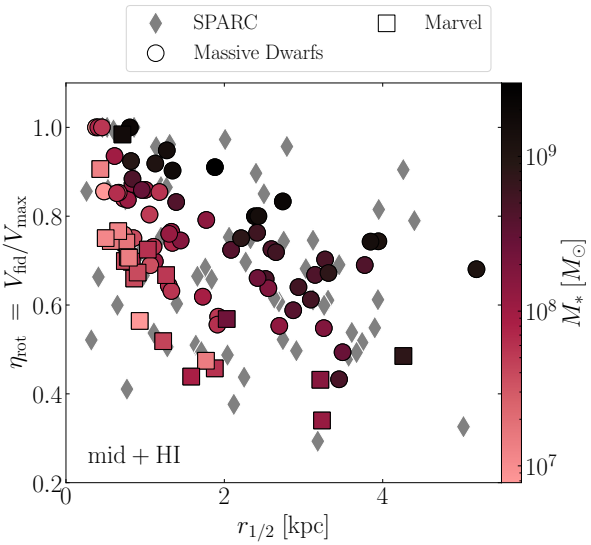


Figure 6. $\eta_{\rm rot}$ versus half-light radius, $r_{1/2}$, colored by M_* for our simulated sample at $z = 0$. The objects that are quickly rising have smaller half-light radii and fractions of mass in dark matter within $r_{1/2}$, meaning they are baryon-dominated. However, there are also objects at lower $\eta_{\rm rot}$ that have smaller sizes because they are less massive. The relationship between $\eta_{\rm rot}$ and $r_{1/2}$ covers a similar region of the $\eta_{\rm rot}$–$r_{1/2}$ plane as the SPARC observations.

has a clear dependence on M_*, as is seen in the gradient from the bottom left to the upper right in Figure 6. Further, at a fixed M_*, there is a clear inverse correlation between $\eta_{\rm rot}$ and $r_{1/2}$, with more steeply rising galaxies being more compact, and more slowly rising galaxies having larger sizes. Thus, the inverse correlation at a fixed M_* is driven by the diversity in galaxy sizes at a given stellar mass. For fixed $V_{\rm max}$ (e.g., galaxy mass), $\eta_{\rm rot}$ can extend over the full range from ∼0.3 to 1 (see Figure 5). Given the size–M_* relation, galaxies with larger stellar masses typically have larger median sizes. When $\eta_{\rm rot} \sim 0.4$, the lower-mass (higher-mass) galaxies will populate the lower (upper) end of $r_{1/2}$ values. The net result is significant scatter in sizes when $\eta_{\rm rot} \lesssim 0.6$. Except for a few objects at the extremes, the simulated sample covers a similar area in the $\eta_{\rm rot} - r_{1/2}$ plane to the SPARC sample, indicated by the gray diamonds.

In addition to struggling to reproduce the diversity of RCs, previous simulation suites have struggled to produce size–M_* relationships consistent with observations. In dwarf galaxies, compact and extended galaxies are observed at a given stellar mass, whereas most simulations with strong feedback only produce the most diffuse objects. On the other hand, simulations with weak feedback also yield galaxies that are too large at fixed stellar mass (D. J. R. Campbell et al. 2017; A. Pillepich et al. 2019). We examine the size–M_* relationship in the Marvel and Massive Dwarf simulations in Figure 7. In the top panel, the SPARC galaxies are shown in gray diamonds, with the Marvel galaxies in teal squares and the Massive Dwarf zooms in purple circles. The size is given in terms of the half-light radius, as outlined in Section 4.3. The bottom panel shows the SPARC galaxies in gray diamonds and galaxies from the NIHAO simulation suite extracted from F. Jiang et al. (2019) as the light blue diamonds. The observed trend for late-type galaxies (LTGs) from A. van der Wel et al. (2011) is shown by the pink solid line, which changes to dashed below $M_* \lesssim 10^9\ M_\odot$, where it is extrapolated. The pink shaded region indicates the 68% containment interval of scatter in the observed relation. We additionally show the observations of ELVES dwarf galaxies

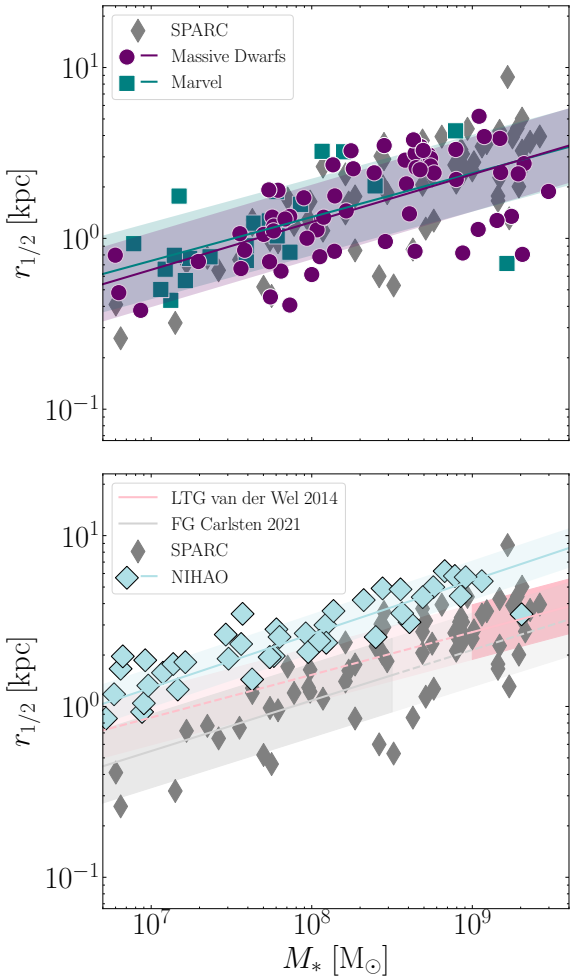


Figure 7. $r_{1/2}$ versus M_*. Top: the Massive Dwarfs are shown in circles, the Marvel dwarfs in squares, and the SPARC galaxies in gray diamonds. Power-law fits are shown for the Massive Dwarfs and Marvel dwarfs in purple and teal, respectively. The Massive Dwarfs and Marvel galaxies cover the same area as SPARC. Bottom: the LTG size–M_* relation for normal-size galaxies is shown in the pink shaded region for $M_* > 10^9\ M_\odot$ (A. van der Wel et al. 2011). The field size–M_* relationship is shown by the light-gray line and shaded region, corresponding to 1σ scatter, for $M_* < 10^{8.5}\ M_\odot$ (S. G. Carlsten et al. 2021). The extrapolation of each observed relation is shown by a dashed line. $r_{1/2}$ versus M_* for the NIHAO simulation suite is shown in the light blue diamonds (F. Jiang et al. 2019). The NIHAO simulated suite size–M_* relationship is offset from the SPARC galaxies, as well as the fitted size–M_* relationships, particularly below $M_* \sim 10^9\ M_\odot$.

with the field size–M_* relationship in light gray for $M_* < 10^{8.5}\ M_\odot$ from S. G. Carlsten et al. (2021). The dashed light-gray line denotes the extrapolation of the relationship above $M_* \gtrsim 10^{8.5}\ M_\odot$. A. van der Wel et al. (2011) examine larger-mass galaxies with $M_* > 10^9\ M_\odot$, whereas S. G. Carlsten et al. (2021) focus on the dwarf regime with $M_* \lesssim 10^{8.5}\ M_\odot$, and each are extrapolated to cover the full range of M_* considered in this work. The S. G. Carlsten et al. (2021) size–M_* relationship overlaps with the SPARC galaxies, but the relationship inferred at higher masses is offset below the SPARC data.

At $M_* \lesssim 10^9\ M_\odot$, the Massive Dwarf zooms and the Marvel galaxies cover a similar area as the SPARC galaxies in the size–M_* plane (the upper panel of Figure 7). In contrast, the NIHAO galaxies are offset from the observed relations (the lower panel). A similar offset is noted for FIRE (though see C. Klein et al. 2024) and galaxies from A. Lupi et al. (2017) in

Table 2
Compact Galaxy Numerical Experiments Varying Subgrid Physics

Test	Resolution	Star Formation	Feedback	Feedback Energy Budget	BHs
1 (fiducial)	Mint	H_2	Superbubble	10^{49} erg $M_\odot^{-1}$	Yes
2	Mint	H_2	Superbubble	10^{49} erg $M_\odot^{-1}$	No
3	Mint	NIHAO	Superbubble	10^{49} erg $M_\odot^{-1}$	No
4	Near Mint	H_2	Superbubble	10^{49} erg $M_\odot^{-1}$	No
5	Near Mint	NIHAO	Superbubble	10^{49} erg $M_\odot^{-1}$	No
6	Near Mint	NIHAO	Blastwave	10^{49} erg $M_\odot^{-1}$	No
7	Near Mint	NIHAO	Blastwave + Early Feedback	10^{49} erg $M_\odot^{-1}$ + 2×10^{50} erg $M_\odot^{-1}$	No

Note. The table lists the resolution of each associated subgrid variation, along with the star formation prescription and feedback model used, as well as the feedback energy budget. The details of the H_2-based star formation model are found in C. Christensen et al. (2012), while the NIHAO star formation parameters are described in L. Wang et al. (2015). The superbubble feedback is described in B. W. Keller et al. (2014), while the BW feedback and early-stellar-feedback models are described in G. Stinson et al. (2006) and G. S. Stinson et al. (2013), respectively. The BH prescription used in our fiducial model is described in M. Tremmel et al. (2015) and M. Tremmel et al. (2017). Each variation is labeled by a test number, given in the first column.

F. Jiang et al. (2019). We fit a power law to the size–M_* relationship as

$$\log_{10}(r_{1/2}/\mathrm{kpc}) = a + b \log_{10}\left(\frac{M_*}{5 \times 10^6 M_\odot}\right) \quad (8)$$

and calculate the scatter σ as the standard deviation of the simulated data from the best-fit line. For the Massive Dwarfs, $a = -0.268$, $b = 0.279$, and $\sigma = 0.218$. Marvel has a slightly shallower slope and larger scatter, with $a = -0.208$, $b = 0.256$, and $\sigma = 0.225$. Both Marvel and the Massive Dwarfs are in fair agreement with S. G. Carlsten et al. (2021),[17] which reports $a = -0.347$, $b = 0.296$, and $\sigma = 0.215$. However, the NIHAO relationship has less scatter and is offset with $a = 0.015$, $b = 0.314$, and $\sigma = 0.116$. For intuition on a, note that the $M_* = 5 \times 10^6 M_\odot$ intercept is 0.450 kpc for the S. G. Carlsten et al. (2021) field galaxy relationship, compared to 0.540 kpc for the Massive Dwarfs and 1.036 kpc for NIHAO.

Previous galaxy formation models in CDM with baryons have failed to produce compact objects below $M_* \sim 10^9 M_\odot$ (F. Jiang et al. 2019; L. V. Sales et al. 2022). Given the relation we have found here between steeply rising RCs and compact sizes (Figure 6), it seems that a failure to make compact objects may be tied to why previous simulations that produce cores have failed to simultaneously reproduce the most quickly rising RCs (I. M. Santos-Santos et al. 2018; I. M. E. Santos-Santos et al. 2020). We find objects as compact and extended as the SPARC galaxies across stellar mass in both the Marvel and Massive Dwarf galaxies, even though cores are also produced. On the other hand, steeply rising RCs can arise from a number of sources. For example, they can be correlated with dark matter cusps (in the absence of compact galaxies as in, e.g., APOSTLE; D. J. R. Campbell et al. 2017; I. M. E. Santos-Santos et al. 2020), compact stellar distributions, and/or centrally concentrated gas distributions.

In R. Geda et al. (2026), we examine the origin of the varying sizes in the Massive Dwarfs. Here, we restrict our analysis to understanding why previous simulations may not have made compact galaxies. We explore this in the next section.

[17] We shift the log y-intercept reported in S. G. Carlsten et al. (2021) (a_c) to account for the unit conversion in log space. Additionally, we shift the relation by $M_* = 5 \times 10^6 M_\odot$, so $a = a_c - 3 + b \log_{10}(5 \times 10^6) = 0.347$, where $a_c = 0.667$.

6. The Role of Subgrid Physics

The simulations studied in this work include both compact and extended objects, in better agreement with observations than previous numerical studies. For example, the sample of galaxies at $M_* \lesssim 10^9 M_\odot$ in NIHAO and FIRE is offset from the observed size–M_* relationship, with all of the objects being more extended (F. Jiang et al. 2019). This section performs a detailed comparison of the Massive Dwarf zoom-in simulations to NIHAO, seeking to identify the source of this difference. We focus on NIHAO because it was run with GASOLINE2 (J. W. Wadsley et al. 2017), which has a similar hydrodynamics code to CHANGA, allowing us to rerun galaxies with different parameter choices to determine their impact.

To perform this comparison, we run controlled experiments on two galaxies, r556 and r618, which are more compact than the 1σ interval of the observed field galaxy size–M_* relationship found in S. G. Carlsten et al. (2021). We attempt to mitigate numerical butterfly effects by ensuring the two galaxies also have quiescent merger histories after $z \sim 2$ (S. Genel et al. 2019; B. W. Keller et al. 2019). B. W. Keller et al. (2019) showed that major mergers (1: 1) can significantly alter the stellar masses in simulations with the same initial conditions and subgrid physics, just rerun many times. Because B. W. Keller et al. (2019) found that sizes are stable to numerical chaos, but morphologies are not, we only focus on differences in size. Beyond this, they showed that galaxies with higher surface densities, like r556 and r618, tended to be more immune to galactic chaos. While we attempt to mitigate these nonlinear effects, they may still impact differences in size and mass as the subgrid physics is varied below.

Table 2 summarizes the six different subgrid physics variations that are considered. The tests are performed in steps from the fiducial model to a subgrid model more closely resembling NIHAO. The fiducial model (see Section 2.2) differs from the NIHAO subgrid model (detailed in Section 2.3) in star formation, feedback, and resolution.

Figure 8 shows the differences in the UVI images due to the subgrid physics variations. The top row shows the variations of simulation r556, and the bottom row shows those of r618. The first column of Figure 8 shows the fiducial model, designated as Test 1 in Table 2. Relative to the full set of galaxies in Figure 1, it is visually apparent that these two are some of the most compact in the Massive Dwarf sample. Figure 9

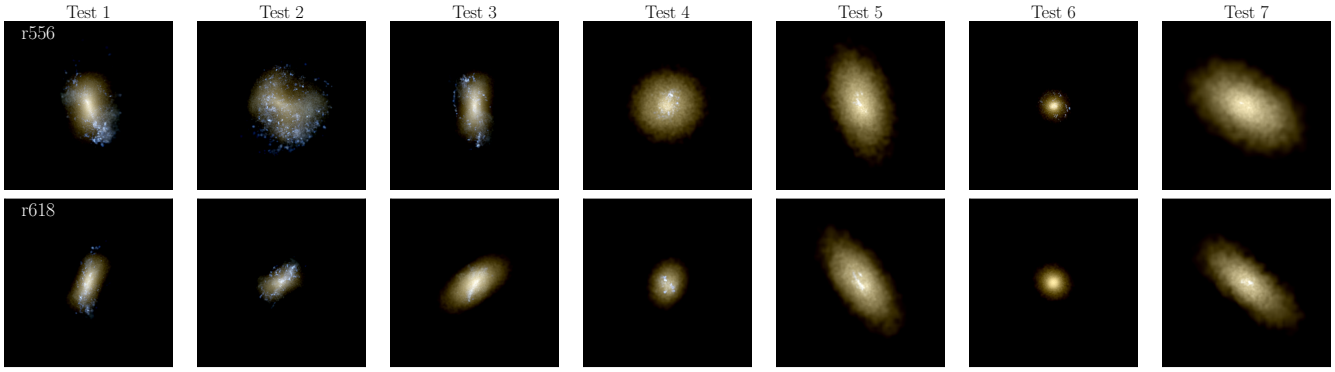


Figure 8. Mock UVI images with different subgrid physics. Each panel has a side length of 15 kpc. The two different rows are for two simulations, r556 and r618, with the following physics in the columns. First: the fiducial H_2 star formation and superbubble feedback. Second: the H_2 star formation with superbubble feedback and no BHs. Third: the NIHAO star formation and superbubble feedback at the fiducial resolution. Fourth, the H_2 star formation with superbubble feedback at Near Mint resolution. Fifth: the NIHAO star formation and superbubble feedback at Near Mint resolution. Sixth: the NIHAO star formation with blastwave feedback. Seventh: the NIHAO star formation with blastwave and early feedback. Test 7 is the closest to the original NIHAO simulation model. See the text for details.

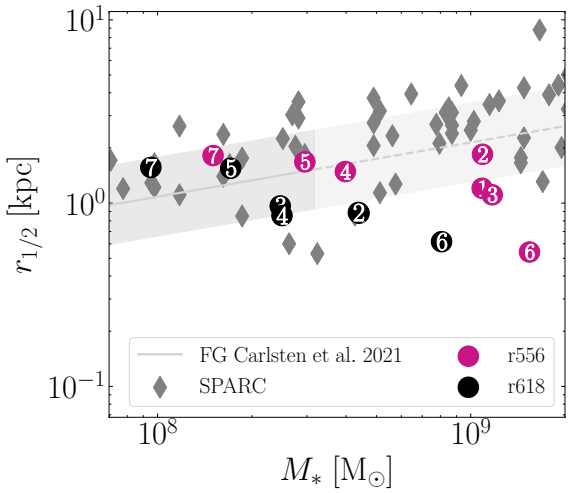


Figure 9. $r_{1/2}$ versus M_* for galaxies r556 (magenta) and r618 (black), run with different subgrid physics. The marker number denotes the particular subgrid physics test from Table 2. We note that Test 1 in r618 is sitting directly under Test 2. The SPARC data are shown by the gray diamonds, and the field size–M_* relationship is shown by the light-gray shaded region for $M_* < 10^{8.5}\,M_\odot$, from S. G. Carlsten et al. (2021), with the extrapolation to higher masses indicated by the dashed line. The compact objects in Test 1 (fiducial model) progressively move from compact galaxies in the lower right of the size–M_* plane to the upper left; $r_{1/2}$ increases, while stellar masses decrease.

quantifies the shifts in the size–M_* plane associated with each subgrid variation, with r556 in magenta and r618 in black, each numbered with the associated test listed in Table 2. Our goal is to understand whether changes that bring the subgrid model in closer alignment to that used by NIHAO also change the compactness of these systems.

6.1. BHs

First, we rerun the fiducial model without BHs. This is done because the NIHAO simulations we compare to do not include BHs. In Milky Way–mass galaxies, the absence of a BH should increase star formation, altering M_* (M. Tremmel et al. 2017); however, the expectations for how intermediate-mass BHs impact dwarf galaxies are less well studied. As was discussed in Section 2.2, J. M. Bellovary et al. (2019) found little BH accretion in the Marvel galaxies, which suggests that there should be little change to $r_{1/2}$ and M_* when BHs are removed. The second column in Figure 8 shows the results of Test 2, in which the only change is removing BHs from the fiducial model. The $r_{1/2}$ remains roughly constant in r618, but it increases by roughly 50% in r556 (see Figure 9). In addition to the two galaxies shown here, we also explored a larger set of Massive Dwarf zoom galaxies with and without BHs and found no preferential shift in the size–M_* plane. The source of this size increase seen for r556 may thus be random, despite attempts to minimize the impact of the merger history. We conclude that there is no clear evidence that BHs are influencing the sizes or stellar masses of these dwarf galaxies.

6.2. Star Formation Model

The third column of Figure 8 (Test 3) builds upon Test 2 by altering the star formation model. As described in Section 2, our fiducial model follows the formation and destruction of H_2 and requires that H_2 be present when stars form. NIHAO uses density and temperature thresholds that allow stars to form at lower densities and higher temperatures than our fiducial model. However, changing the star formation model at this resolution does not preferentially alter the stellar half-light radius of each galaxy, as r556 becomes smaller (returning to roughly the size of the fiducial run) and r618 becomes larger (though only by $\sim$10%). In other words, there is no clear evidence that changing the star formation prescription substantially impacts sizes at the fiducial Mint resolution.

However, we do find differences when going to lower resolution that we believe are influenced by the star formation model (discussed below). Hence, while we conclude that the star formation scheme yields similar size galaxies at the fiducial resolution, we caution the reader that this might not be applicable under all circumstances.

6.3. Resolution

Since the mass resolution of the NIHAO galaxies in this halo mass range is lower than our fiducial resolution, we additionally explore tests at lower, Near Mint resolution (see Section 2.3 for the spatial and mass resolution details). The fourth column of Figure 8 shows the results of Test 4, which is identical to Test 2, but at Near Mint resolution—i.e., it is our fiducial model, minus BHs, but at lower resolution. Compared to the second column of the figure, the stellar sizes show no

preferential change: r556 becomes ∼20% larger, and r618 stays roughly the same.

Keeping the Near Mint resolution the same but changing to the NIHAO star formation model (Test 5) results in larger stellar sizes compared to Test 4. The same is true when comparing the results of Test 5 to those of Test 3 (which has the same physics, but at the higher Mint resolution). We conjecture that the change in size is due to the fact that a star formation model based on a density threshold is inherently resolution-dependent. In the NIHAO star formation model, stars start to form right when the gas density crosses the star formation density threshold $n_* \geqslant 10.3$ cm^{-3} at both resolutions. As the resolution is lowered, the simulation loses the ability to resolve high-density peaks of gas. For reasons that are not understood, the lower resolution results in stars at larger radii (as can be seen in Figure 8). While the H_2 star formation model is not fully immune to resolution effects, the requirement that H_2 be present for star formation may act to keep sizes more stable, because it limits star formation to regions with high densities, $n_* \geqslant 100$ cm^{-3}. A full understanding of these effects requires additional work beyond the scope of this paper.

In summary, the NIHAO star formation model does lead to slightly larger galaxies at lower resolution, unlike our fiducial model. However, the change is not dramatic enough to explain the sizes of the dwarfs seen in NIHAO.

6.4. Feedback

NIHAO also utilizes different feedback. The remaining two tests switch from superbubble feedback to blastwave. Test 6 is the same as Test 5, except for this one change. As is immediately obvious from the sixth column of Figure 8, the galaxies become much more compact after this switch. The reduction in size is in agreement with M. Mina et al. (2021), who found that dwarf galaxies simulated with blastwave feedback result in galaxies that have 2–3 times smaller $r_{1/2}$ than the same systems run with superbubble. They conjecture that superbubble more strongly fluctuates the gravitational potential, which expands the radii of both dark matter (making cores) and stars, since both are collisionless particles (see, e.g., A. S. Graus et al. 2019; C. L. Riggs et al. 2024). However, sizes were *not* found to be different between the two feedback models in B. Azartash-Namin et al. (2024). While M. Mina et al. (2021) adopt a density threshold for star formation, B. Azartash-Namin et al. (2024) adopt the same H_2-based star formation as our fiducial model. This suggests again that the change in size may be dependent on the star formation model. However, it is clear that a change in feedback can yield dramatic size differences for a given galaxy.

Test 7 is the closest to the NIHAO simulations in L. Wang et al. (2015). Here, we add early stellar feedback to the physics of Test 6, as described in Section 2.3. The stellar sizes increase dramatically from Test 6, resulting in the largest galaxies across all the tests. As mentioned in Section 2.3, the early feedback model is tuned to limit star formation to agree with the abundance-matching value at the Milky Way scale, neglecting the impacts on dwarf scales. This choice may be causing $r_{1/2}$ to be large below $M_* \sim 10^9\,M_\odot$ (the bottom panel of Figure 7). Beyond this, early feedback is added as thermal energy, similar to feedback from SNe II, though cooling is not shut off. This effectively gives a 20 times boost (see the feedback energy budgets in Table 2) to the total SN energy per star particle. Additionally, the energy is injected in a short time period, which likely helps maximize the effect. Given the change from Test 6 to Test 7, we conclude that the early feedback is the strongest contributor to making diffuse galaxies in NIHAO.

6.5. Summary: Changes in the Size–Mass Plane

Figure 9 presents the size–M_* relationships for galaxies r556 (magenta) and r618 (black) as each undergoes variations in its subgrid physics, following Table 2. Each test's position in the size–M_* plane is plotted with its associated number. (Note that Test 1 in r618 is sitting directly under Test 2 in the figure.) The SPARC data are shown in the gray diamonds, and we again present the observed size–M_* relationship with 1σ in the shaded region from S. G. Carlsten et al. (2021), with the line styles as in Figure 7. The Mint resolution runs (Tests 1–3) cluster on the small side of the S. G. Carlsten et al. (2021) median relation, with some scatter. The Near Mint test with superbubble feedback and H_2 (Test 4) does not change much in size, though the stellar mass of r556 decreases, moving closer to the mean size–M_* relation. Switching to the NIHAO star formation scheme increases $r_{1/2}$ and further decreases the stellar mass (Test 5), but switching to blastwave feedback (Test 6) makes the most compact galaxies, indicating that resolution alone is not limiting the production of compact galaxies. Including early feedback as in NIHAO makes the galaxies the most diffuse, while also decreasing their stellar mass (Test 7).

We have not reproduced the most diffuse NIHAO galaxies in the size–M_* plane, but we have reproduced the most compact of the NIHAO galaxies (the lower panel of Figure 7). Additionally, we have not achieved a perfect match to NIHAO with our Near Mint runs, but only stepped in that direction (e.g., our particle masses and gas force resolution are slightly larger than theirs, our early feedback is a bit weaker, and we do not adopt a different, lower force resolution for the dark matter as they do). Test 6 makes it clear that resolution is not limiting the formation of compact galaxies. Further, given that the early feedback has the largest impact on size and stellar mass in our tests, we expect that increasing the early feedback efficiency from the value used here ($\epsilon_{\rm EF} = 10\%$) to the value used in L. Wang et al. (2015) ($\epsilon_{\rm EF} = 13\%$) would further increase sizes and decrease stellar masses. Still, the shift toward the upper left of the size–M_* plane is significant (M_* differs by 1 dex between Test 1 and Test 7 in r618), and the galaxies are nearly off the median relationship. The larger driver from the bottom right to the upper left of the size–M_* plane seems to be due partially to a resolution-dependent star formation model, in addition to very strong early stellar feedback. We conclude that the strong early feedback in NIHAO may prevent the formation of the most compact galaxies.

7. Discussion

Until now, high-resolution simulations of galaxy formation have not been able to reproduce the full diversity of RCs in dwarf galaxies, at least before turning the simulated galaxies into mock observations of RCs (F. A. Roper et al. 2023). Our simulations are able to create dwarf galaxies that rise both more quickly and more slowly than predicted by an NFW profile, as measured by the midplane gravitational potential (the bottom panels of Figure 3). The next subsections will

discuss reasons why we might miss the most extreme objects. However, it is clear that the simulations presented here span a broader range of RC shape diversity than previously seen.

There has been a debate about whether feedback from baryons can solve the RC diversity problem. For example, L. L. R. Williams et al. (2025) predict dark matter density profiles within CDM using a theoretical model based on statistical mechanics. Their model shows that maximum entropy solutions for cold collisionless self-gravitating dark matter halos can have a range of inner density profiles, including flat density cores. They conclude that CDM density profiles can reproduce the whole range of diversity, without considering the contribution from baryons. On the other hand, A. Del Popolo et al. (2018) also used a large set of analytical spherical collapse models to predict dark matter density profiles. Their models include the impact of baryonic feedback on dark matter density profiles. They conclude that the RCs follow the baryonic distribution, though we note that they still struggled to produce objects with the most quickly rising RCs in the $V_{\rm max} \sim 70$–$100\,{\rm km\,s^{-1}}$ range.

In galaxy simulations, the consensus to this point has been that baryons are responsible for creating the most slowly rising RCs in CDM, via the creation of dark matter cores from baryonic feedback (C. B. Brook 2015; I. M. Santos-Santos et al. 2018; I. M. E. Santos-Santos et al. 2020; R. A. Jackson et al. 2025). However, to date, no one has been able to simultaneously create dark matter cores and the most steeply rising RCs at a given mass. These troubles have led to questions about whether baryonic feedback within CDM can produce the full range of diversity (M. Kaplinghat et al. 2020).

We conclude that the ability to simultaneously make quickly rising RCs requires stars to be able to form centrally, without the gas first being removed or puffed up by feedback. To form dwarfs with high surface densities, gas must be allowed to cool and form stars at the centers of halos, without being removed by strong feedback. The ability of the Marvel and Massive Dwarf simulations to simultaneously collect cold gas at their centers while also resolving clustered, bursty star formation allows them to capture a broader range of RC shape diversity in the absence of mock RCs. In particular, these simulations create dark matter cores while still allowing for steep RCs in compact galaxies.

7.1. Observational Considerations

While the simulations in this work produce a broader range of RC shapes than previous simulations, they still do not reproduce all the steeply rising RCs seen in SPARC galaxies with low baryon mass fractions, as well as some of the most slowly rising RCs in SPARC. This subsection speculates how the inclusion of observational effects might impact these specific cases.

Many previous works have examined the origin of noncircular gas motions and their impact on the observed RCs (e.g., O. Valenzuela et al. 2007). The feedback produced by bursty star formation histories in dwarf galaxies can drive them out of dynamical equilibrium (e.g., J. I. Read et al. 2016a; K. El-Badry et al. 2017; R. Verbeke et al. 2017; E. R. Downing & K. A. Oman 2023; I. S. Sands et al. 2026). Clustered SNe can create H I holes (J. I. Read et al. 2016b) inside galaxies, which can be hard to detect, depending on the inclination angle (see also R. Verbeke et al. 2017; I. S. Sands et al. 2026), and feedback also drives noncircular motions, such as turbulence or outflows. On top of feedback-induced noncircular motions, A. Marasco et al. (2018) showed that triaxial halos can induce radial gas flows (bars) in dwarf galaxies (see also K. A. Oman et al. 2019). The analytically derived RC speeds in triaxial halos deviate from spherical halos (see J. Binney & S. Tremaine 2008; J. Bovy 2026). Gas can also experience pressure support that reduces the velocity relative to stars and dark matter (J. J. Dalcanton & A. M. Stilp 2010; J. C. B. Pineda et al. 2017; K. A. Oman et al. 2019; I. S. Sands et al. 2026). Finally, because the relative contribution of rotational velocity is expected to decrease with decreasing galaxy mass, galaxies instead become dominated by dispersion and their disk thickness increases (K. A. Oman et al. 2019; P. E. Mancera Piña et al. 2022). This effect is likely to matter only in the lowest-mass galaxies, rather than our most-massive dwarfs, where diversity is maximized. However, the presence of dispersion, at all galaxy masses, is another factor that would lower the observed rotation velocities (e.g., E. D. Jahn et al. 2023).

Many of the noncircular motions mentioned above may lower the velocities, particularly $V_{\rm fid}$, relative to what we have presented here (K. A. Oman et al. 2019; E. R. Downing & K. A. Oman 2023). $V_{\rm fid}$ may be lowered because many of the processes discussed above are more centrally located, e.g., star formation rates are higher at the centers of galaxies, leading to more clustered star formation, feedback, and turbulence at the centers of galaxies. $V_{\rm max}$ can be lowered as well, but the result would be to shift $r_{\rm fid}$ to smaller radii and thus lower $V_{\rm fid}$ again.

If $V_{\rm fid}$ were to be lowered in mock observations, we can conjecture how our results would change (assuming that $V_{\rm max}$ is largely unaffected). First, we would observe a broader range of $V_{\rm fid}$ in Figure 3 to lower velocities. The most slowly rising RCs are most likely to *appear* slowly rising, due to noncircular motions (K. A. Oman et al. 2019; F. A. Roper et al. 2023). Second, lowering $V_{\rm fid}$ while keeping $V_{\rm max}$ unchanged will lower $\eta_{\rm rot}$. While $\Sigma_{\rm bar}$ is not impacted (since the half-mass radius does not change), lowering $\eta_{\rm rot}$ might help to fill the space across all $\Sigma_{\rm bar}$ in the right panel of Figure 4. Finally, F. A. Roper et al. (2023) have already shown that lower $V_{\rm fid}$ shifts galaxies to lower $\eta_{\rm rot}$ and higher $\eta_{\rm bar}$—i.e., galaxies shift into the lower-right corner in Figure 5.

While the most likely outcome of noncircular motion is a lowering of $V_{\rm fid}$, F. A. Roper et al. (2023) also showed some instances where $\eta_{\rm rot}$ could increase. In particular, bisymmetrical noncircular motions (i.e., bars), such as those introduced within a triaxial halo, lead to sinusoidal variations in $\eta_{\rm rot}$ as the azimuthal viewing angle changes (see their Figure 8). In some viewing angles, $\eta_{\rm rot}$ is much larger than the intrinsic value. We reproduce several galaxies with the steepest $\eta_{\rm rot}$, but they tend to have lower $V_{\rm max}$ values than the SPARC data points with such high $\eta_{\rm rot}$. While this might be simply small number statistics, it could be that such radial motions might bring some of our galaxies as high as the SPARC sample. The simulated galaxies predominantly reside in triaxial halos below $M_\star < 10^8\,M_\odot$ (B. Keith et al. 2025), and we have witnessed the existence of bars in some of them (to be explored further in future work). Such radial motions might cause the most extreme steeply rising RCs.

7.2. The Role of Resolution

In this subsection, we explore how the ratios of dark matter to baryon particle mass impact RCs and stellar sizes. Numerical work has been conducted to examine where artificial two-body relaxation impacts central dark matter density profiles (C. Power et al. 2003; A. D. Ludlow et al.

2019a). Cosmological simulations often include mixtures of heavier dark matter and lighter baryonic particles. The unequal masses can result in so-called "mass segregation,"[18] as the particles try to reach energy equipartition, causing the more-massive particles to lose energy and fall inward, while the lower-mass particles heat up (A. D. Ludlow et al. 2019b).

In simulations where the stellar particles are less massive than their dark matter counterparts, stellar sizes can be artificially extended for low-mass systems at $z = 0$ (A. D. Ludlow et al. 2019b). The simulations presented in this work have large mass ratios between dark matter and stars: $\mu = m_*/m_{\rm DM} \sim 18$ for the Massive Dwarf zooms and $\mu \sim 15.8$ for the Marvel galaxies. This is because stars form with 30% of the mass of their parent gas particles. A. D. Ludlow et al. (2019b) found that the convergence radius $r_{\rm conv}$ for two-body scattering, rather than the gravitational softening, sets the smallest stellar sizes obtainable. They additionally found that convergence was attained at all z when the stellar sizes exceeded $r_{\rm conv}$. All the galaxy sizes in our simulation suites are larger than $r_{\rm conv}$, as calculated in Section 4.2, which indicates that the stellar sizes should be converged.[19]

RCs are also influenced by large mass ratios between dark matter and star particles, because of mass segregation. A. D. Ludlow et al. (2019b) found that dark matter RCs were only marginally impacted for large mass ratios ($\mu > 1$). However, the RCs associated with the stellar components were more significantly affected, with the inner stellar RC decreasing in velocity over time as the stellar component expands relative to the $\mu = 1$ case (see Figure 1 of A. D. Ludlow et al. 2019b).

Dark matter dominates the majority of our RCs at all radii. Larger μ values have little impact on the dark matter contribution to the RC. On the other hand, the most rapidly rising RCs in our sample are dominated by stars (see the density profiles in Appendix C), and the baryonic component of RCs is strongly impacted by mass segregation. In the absence of mass segregation, RCs would rise even more quickly, particularly in the systems dominated by stars in the central regions. Hence, while mass segregation could be lowering $V_{\rm fid}$ in these galaxies, it does not negate the conclusion that we can make steeply rising RCs and hence that we can make a broader range of RC diversity than previous hydrodynamical simulations within CDM.

8. Summary and Conclusions

This paper has explored the diversity of dwarf galaxy properties in 85 simulated galaxies from the Massive Dwarf zoom ins and the Marvel Dwarf zoom volumes. We have compared the properties of their simulated RCs and sizes to SPARC data (F. Lelli et al. 2016a). We found RCs that span a broader range of diversity than previously seen in ΛCDM simulations with baryons.

We explored the shapes of RCs, considering both the true halo $V_{\rm max}$ and that inferred when H I is resolved out to 1 $M_\odot$ pc^{-2}. For the Massive Dwarfs, we find RCs that rise both slower and faster than the NFW prediction for $V_{\rm max} \gtrsim 60$ km s^{-1} when RCs are calculated using the gravitational midplane potential instead of the mass enclosed.

We also found for the first time that the simulated galaxies are a better match to the stellar size–M_* relationship, in contrast with previous simulations, which showed an offset in the size–M_* plane by $\gtrsim$1–2 kpc, with simulated galaxies more diffuse than observed (F. Jiang et al. 2019). Instead, we found dwarf galaxies from the Massive Dwarfs with diverse sizes at a fixed stellar mass, covering a similar area in the size–M_* plane as the SPARC galaxies and having similar power-law slopes, scatters, and offsets to the S. G. Carlsten et al. (2021) size–M_* power-law relationship.

We examined whether RC shapes are correlated with baryonic distributions, as previous works have drawn differing conclusions on this topic. We found the correlation varies with $V_{\rm max}$. In a fixed bin of higher $V_{\rm max}$, the most quickly rising RCs belong to more compact, high-baryonic-surface-density galaxies, and the most slowly rising RCs occurred in lower-baryonic-surface-density galaxies. This is in agreement with previous work by T. Ren et al. (2019). However, this was not true for lower-$V_{\rm max}$ systems, which showed a larger spread in RC shapes (measured by $\eta_{\rm rot}$) at a fixed baryonic surface density, in line with I. M. E. Santos-Santos et al. (2020). We found significant diversity at lower surface densities and low baryon mass fractions within $r_{\rm fid}$.

By rerunning two of our most compact galaxies, we conclude that the early stellar feedback used in the NIHAO simulations likely prevents the formation of the most dense galaxies, leading to galaxies that are more diffuse than those observed (F. Jiang et al. 2019). I. M. E. Santos-Santos et al. (2020) showed that their EAGLE-CHT10 model, which has clustered, bursty star formation leading to dark matter cores, also makes diffuse dwarf galaxies and none that are more quickly rising than NFW below $V_{\rm max} \sim 100$ km s^{-1} (see also F. A. Roper et al. 2023). Although we were unable to rerun their models, it seems clear that they likely also have feedback strong enough to prevent the formation of compact galaxies.

However, steeply rising SPARC RCs with low baryon mass fractions and higher $V_{\rm max}$ are missing from our sample. There is also a subset of the most slowly rising SPARC RCs with large baryon mass fractions that we were unable to reproduce, and this is apparent in multiple galaxy property planes. The existence of these slowly rising RCs with large baryon mass fractions and high surface densities remains physically perplexing. Simulations with stronger feedback do a better job of populating this region, but at the expense of making steeply rising RCs and the most compact observed dwarf galaxies. Additionally, even the models with the strongest feedback still struggle to produce the most slowly rising RCs (I. M. E. Santos-Santos et al. 2020; R. A. Jackson et al. 2025), which are also missing from our sample. We postulate that the RCs of these systems may be impacted by noncircular motions, as found using mock H I RCs in F. A. Roper et al. (2023). We also note that works generating mock RCs should ensure and report that they are also able to properly produce the size–M_* relationship in dwarf galaxies, to fully address the diversity of dwarfs problem. We do not perform a similar mock analysis in this paper, but hope to in future work.

We conclude that the ability to simultaneously make quickly rising RCs requires gas to form stars at the centers of simulated galaxies without first being blown out by feedback. To form dwarfs with high surface brightnesses, gas must be allowed to cool and form stars at the centers of halos, without being removed by strong feedback that can also make them puffier.

[18] This nomenclature is taken from A. D. Ludlow et al. (2019b).

[19] B. Azartash-Namin et al. (2024) showed that the stellar sizes in Marvel galaxies stop changing at $r_{1/2} \sim 0.34$ kpc—smaller than the galaxies we consider here, but consistent with A. D. Ludlow et al. (2019b).

However, this process is not fully understood, and further investigation is warranted. The ability of these CHANGA dwarfs to simultaneously collect cold gas at their centers while also resolving clustered, bursty star formation allows them to capture a broader range of size and RC diversity. In particular, these CDM simulations create dark matter cores while still allowing for steep RCs in compact galaxies.

It has also been argued that the diversity of RC shapes is better reproduced in a self-interacting dark matter (SIDM) model (D. N. Spergel & P. J. Steinhardt 2000) than in CDM (M. Kaplinghat et al. 2014, 2020; T. Ren et al. 2019). Assuming a low SIDM cross section allows dwarfs in this mass range to produce thermalized dark matter density cores that react to the potential of the baryonic distribution. In this model, RC shapes correlate with high- and low-surface-brightness galaxies. However, the absence of the most compact objects in previous simulations will make producing diversity impossible for galaxies simulated in this SIDM case, as well as in the CDM case. We will explore this in a forthcoming work.

Acknowledgments

A.C. thanks Julianne Dalcanton, Nico Garavito Camargo, Adrian Price-Whelan, and Isabel Santos-Santos for helpful discussions on this work. A.M.B. acknowledges support from NSF grant AST-2306340 and from grant FI-CCA-Research-00011826 from the Simons Foundation. M.L. is supported by the Department of Energy (DOE) under Award No. DE-SC0007968 and the Simons Investigator in Physics Award. A.H.G.P. is supported by National Science Foundation grant Nos. AST-2008110 and AST-2510899. F.D.M. acknowledges support from NSF grant PHY2013909. This research was supported in part by grant NSF PHY-2309135 to the Kavli Institute for Theoretical Physics (KITP). This work was performed in part at the Aspen Center for Physics, which is supported by National Science Foundation grant PHY-2210452. B.W.K. acknowledges support provided by NASA through a grant from the Space Telescope Science Institute, through grant HST AR-17547. This work used Stampede2 at the Texas Advanced Computing Center (TACC) through allocation MCA94P018 from the Advanced Cyberinfrastructure Coordination Ecosystem: Services & Support (ACCESS) program, which is supported by U.S. National Science Foundation grants 2138259, 2138286, 2138307, 2137603, and 2138296. Resources supporting this work were provided by the NASA High-End Computing (HEC) Program through the NASA Advanced Supercomputing (NAS) Division at Ames Research Center. Some of the simulations were performed using resources made available by the Flatiron Institute. The Flatiron Institute is a division of the Simons Foundation.

Appendix A
Comparison of RC Shape Measurement Methods

The main text presents four different ways of measuring the maximum and central velocities, $V_{\rm max}$ and $V_{\rm fid}$. Here, we present a direct comparison between methods for each of the Massive Dwarf zoom galaxies. We first compare how the midplane method for deriving RCs and the spherical mass-enclosed method (Equations (4) versus (3)) impact the results in the $V_{\rm fid}$–$V_{\rm max}$ plane. The left panel of Figure A1 compares the mid method in dark purple to the circ method in light purple, with a black line connecting the same galaxy measured with the two different approaches. If the galaxy has a stellar disk, it is denoted with an "X" marker; if it does not have a disk, it is marked with a circle. We use the specific angular momentum j of the stars to define disks. After aligning the galaxy in the x–y plane using the angular momentum vector of the gas in the central 5 kpc, galaxies with a median stellar z-component $j_z/j > 0.5$ are defined as disks. We find that galaxies with disks have larger $V_{\rm max}$ and lower $V_{\rm fid}$ values when

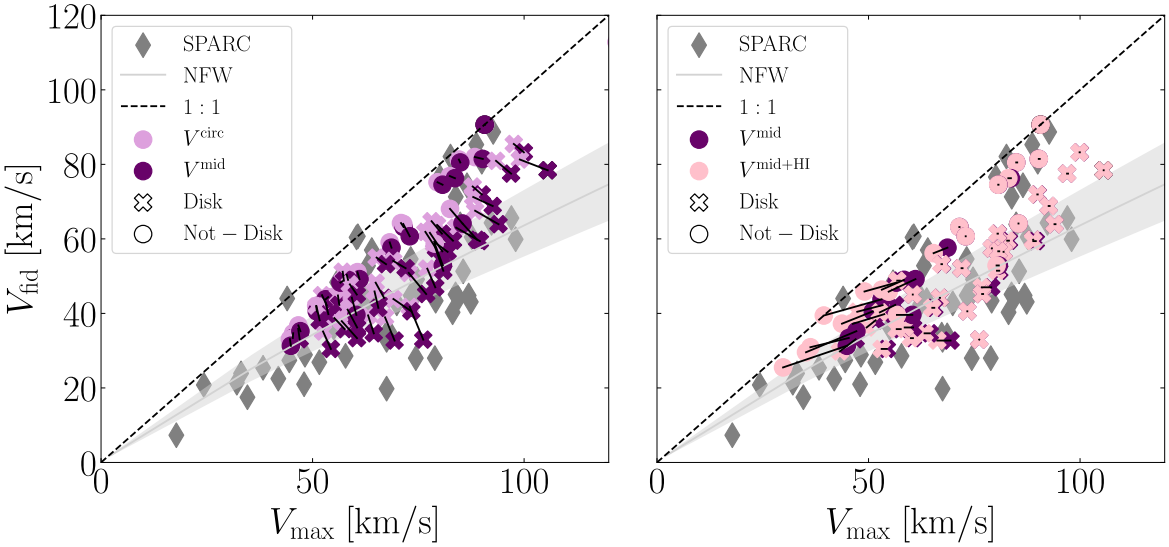


Figure A1. RC shape measurement comparison for the Massive Dwarf galaxies. In both panels, the SPARC galaxies are shown in the gray diamonds, the NFW prediction is the gray shaded region corresponding to the scatter in the mass–concentration relationship, and the black dashed line is the 1: 1 line. Additionally, the disk galaxies are denoted with "X" markers and the galaxies that are not disks are shown as circles. Left: a comparison between the mid method (dark purple) and the circ method (light purple) is shown. When disks are present, the Massive Dwarfs shift to lower $V_{\rm fid}$ and larger $V_{\rm max}$ for the mid compared to the circ method. Right: a comparison between the mid+HI method (pink) and the mid method (dark purple) is shown. For the higher-mass systems, there is little change between the two methods, and it is only at the low-$V_{\rm max}$ end where galaxies start to have lower $V_{\rm max}$ and $V_{\rm fid}$ for the mid+HI compared to the mid case. This is because in the H I case, the RC is still rising at R_1, causing a shift to lower $V_{\rm max}$. This shift causes $r_{\rm fid}$ to be measured at a lower radius along the same RC curve, decreasing $V_{\rm fid}$.

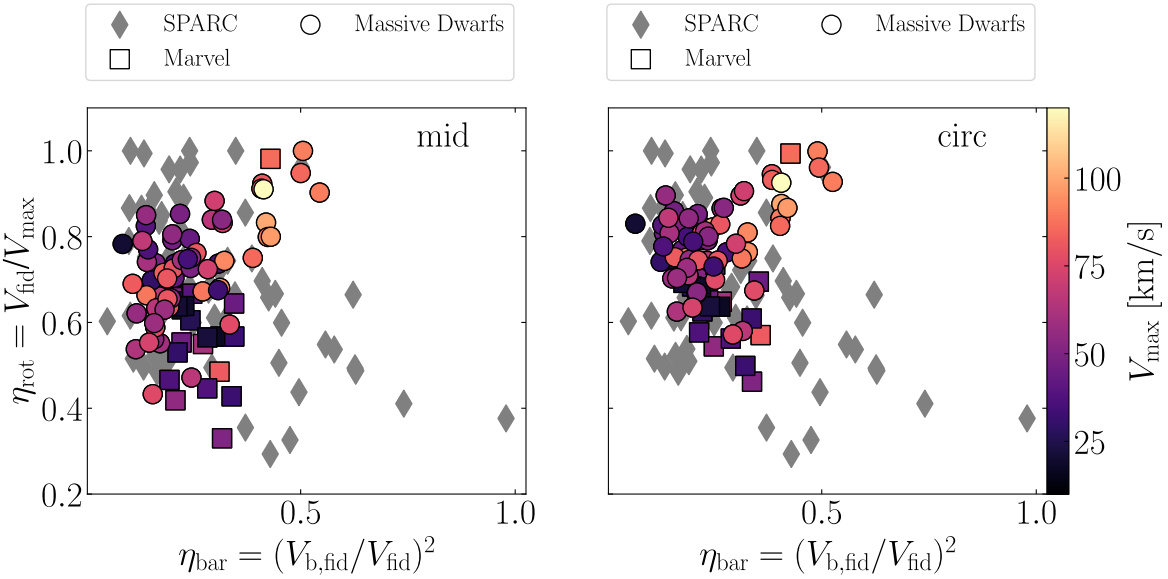


Figure A2. $\eta_{\rm rot}$ versus baryon mass fraction within $r_{\rm fid}$, colored by $V_{\rm max}$. Left: the Massive Dwarf zooms are shown in circles and the Marvel sample in squares, using the mid method to calculate velocities. Most of the simulated galaxies have $\eta_{\rm bar} \lesssim 0.5$. There is a spread in $\eta_{\rm rot}$ in this region, but no systems with $\eta_{\rm rot} \gtrsim 0.75$, higher than the NFW prediction. Right: the Massive Dwarf zooms are shown in circles and the Marvel sample in squares, using the circ method to calculate velocities. The spread is suppressed when using the circ method, because the midplane potential method and the observational limits of H I enhance the spread in $\eta_{\rm rot}$ and $\eta_{\rm bar}$.

mid is compared to circ. This is in agreement with the analytic prediction that RCs derived for disks using gravitational potentials peak at larger velocity and galactocentric radius compared to the spherical mass-enclosed case. Thus, disk galaxies shift to the lower right of the $V_{\rm fid} - V_{\rm max}$ plane, sometimes falling below the NFW prediction when the mid (or mid+HI) method is used. Nondisks also shift, with lower-$V_{\rm max}$ systems shifting more in $V_{\rm fid}$ than $V_{\rm max}$. As we discuss in the main text, this is likely due to the fact that the feedback in lower-mass galaxies can easily throw them out of dynamical equilibrium.

The right panel of Figure A1 compares the case where RCs are measured out to the true $V_{\rm max}$ versus that of truncating the RCs at R_1 to mimic observational limits. Most velocity measurements are unaffected above $V_{\rm max} \sim 60$ km s^{-1}. For the lower-mass systems, the galaxies shift to the lower left of the $V_{\rm fid} - V_{\rm max}$ plane, closer to or at the 1: 1 line, when the mid +HI method is used instead of the mid method. In the lower-mass systems, R_1 decreases (see D. Ruan et al. 2025). The smaller R_1 leads to a decrease in the measured $V_{\rm max}$. Thus, $r_{\rm fid}$ decreases, since it is proportional to $V_{\rm max}$, and $V_{\rm fid}$ also decreases.

We further compare how the different ways of measuring velocities impact the spread of simulated galaxies in the $\eta_{\rm rot} - \eta_{\rm bar}$ plane. The left panel of Figure A2 shows the relationship using the mid method; the objects with a low baryon mass fraction that had steeply rising RCs in the mid +HI case are no longer present. As discussed in the main text, these objects exist in the mid+HI case because they are low-mass systems with low R_1, which makes the RCs look more steeply rising than they would be if the RCs were observed out to larger galactocentric distances. The right panel of Figure A2 shows the relationship using the circ method; the spread is further suppressed, as the mid method better captures the impact of a disk compared to the circ method. In particular, the circ method tends to have lower $V_{\rm max}$ compared to the mid method, as demonstrated in the left panel of Figure A1.

Appendix B
The Impact of Superbubble versus Blastwave Feedback

B. Azartash-Namin et al. (2024) explored differences in the burstiness of star formation and the impact on dark matter density profiles in superbubble compared to blastwave feedback for the Marvel volume Storm galaxies. They also explored additional galaxy scaling relations. We select the galaxies in both Storm zoom volumes that match our stellar mass cut, and we match each halo in the two different runs using dark matter particle IDs, as detailed in B. Azartash-Namin et al. (2024). In Figure B1, we show the pairs with the matches connected with black lines. The superbubble runs are shown in maroon and the blastwave runs in black. The mid+HI method is used in both cases. There is a preference toward larger $V_{\rm max}$ for a given galaxy in the runs with superbubble feedback. B. Azartash-Namin et al. (2024) noted a systematic increase in $M_{\rm vir}$ in the superbubble runs compared to the blastwave runs, likely translating to the preference for larger $V_{\rm max}$ in the superbubble compared to the blastwave runs. For the lower-mass systems, the RCs are pushed toward or above the NFW prediction shown by the gray line. In the most-massive system, however, only $V_{\rm max}$ increases.

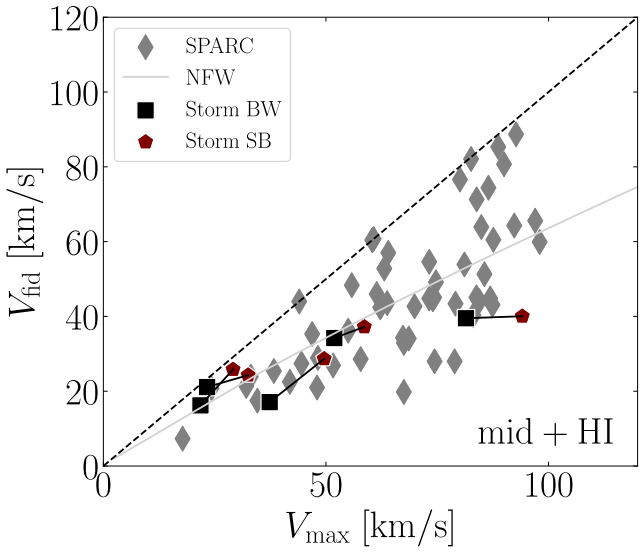


Figure B1. $V_{\rm fid}$ versus $V_{\rm max}$ comparison in galaxies run with superbubble (maroon pentagons) versus blastwave feedback (black squares), with the SPARC data shown by the gray diamonds and the NFW prediction in gray. The black lines connect the same halo in the blastwave versus superbubble cases. There is a preference for higher $V_{\rm max}$ for galaxies with superbubble compared to those with blastwave feedback.

Appendix C
Density Profiles

Figure C1 shows the density profiles (outside the convergence radius $r_{\rm conv}$) for the 30 most-massive galaxies in the Massive Dwarf set. Using the simulation particle data, we show the spherically averaged densities for dark matter, gas, and stars in red, maroon, and orange, respectively. The subpanels are ordered by M_* from top to bottom and left to right in a given row, with the simulation name given in the upper-right-hand corner of each subpanel. The value of $r_{\rm fid}$ is indicated by the dashed black vertical line in each subpanel.

We fit all $z = 0$ dark matter density profiles to a core Einasto profile (A. Lazar et al. 2020):

$$\log\left[\frac{\rho_{\rm cEin}(r)}{\rho_s}\right] = -\frac{2}{\alpha_\epsilon}\left[\left(\frac{r + r_c}{r_s}\right)^{\alpha_\epsilon} - 1\right], \tag{C1}$$

where ρ_s is a normalization parameter, r_c is the core radius, r_s is the scale radius, and $\alpha_\epsilon = 0.16$. We restrict the density profile fits to the radial range of $r_{\rm conv}$ to R_{200}. The lower bound is intended to limit artificial two-body heating at low radii (C. Power et al. 2003; A. D. Ludlow et al. 2019a).

Following A. Lazar et al. (2020), we quantify the goodness of fit using the quality factor, Q, defined as

$$Q^2 = \frac{1}{N}\sum_i^N [\log_{10}\rho_i - \log_{10}\rho_i^{\rm fit}]^2 \ , \tag{C2}$$

where N is the number of radial bins, and $\rho^{\rm fit}$ is the fit defined using Equation (C1) with the relevant parameters chosen to minimize Q. The best-fit core Einasto curve is shown as the dashed black curve in each subpanel of Figure C1.

The slope of the dark matter density profile is

$$\frac{dlog\ \rho_{\rm cEin}(r)}{dlog\ r} = -2\left(\frac{r}{r_s}\right)^{\alpha_\epsilon}\left(1 + \frac{r_c}{r}\right)^{\alpha_\epsilon - 1}, \tag{C3}$$

and it is related to the inner slope of the RC—i.e., the shape of the inner RC. More explicitly, halos with central densities with slope α ($\rho \sim r^\alpha$) have central mass profiles

$$M(r) \sim \int_0^r dr' r'^\alpha r'^2 \sim r^{3+\alpha}, \tag{C4}$$

and the associated spherical mass-enclosed circular velocity profiles rise as

$$V_{\rm circ} \sim \sqrt{r^{3+\alpha}/r} \sim r^{1+\alpha/2}\,. \tag{C5}$$

When a disk is present, it will dominate the midplane potential, further altering the shape of the RCs (J. Binney & S. Tremaine 2008). As noted in K. A. Oman et al. (2015), the size of the core also influences the shape of RCs, since $V_{\rm circ}$ depends on the mass enclosed.

Figure C2 explores how the dark matter slope $\alpha(r_{\rm fid})$ is related to the RC shape parameter $\eta_{\rm rot}$, with the points colored by the dark matter mass fraction within $r_{1/2}$, $f_{\rm DM}(r_{1/2})$. There is a clear correlation between $\eta_{\rm rot}$ and $\alpha(r_{\rm fid})$. The most slowly rising objects have $\alpha(r_{\rm fid}) \sim -0.5$, while the most quickly rising objects have $\alpha(r_{\rm fid}) \lesssim -1.5$. The latter also have the smallest dark matter fractions; in these cases, prominent central stellar distributions dominate the total inner densities, setting the central velocities (Figure C1).

We also check the slopes in the corresponding DMO Massive Dwarf zooms using the same fitting methods. These simulations have the same cosmology, gravitational softening, and dark matter particle-mass resolution as the hydro Massive Dwarf zooms. Measuring the slope at $r_{\rm fid}$ of the corresponding hydro run, we find $\alpha(r_{\rm fid}) \sim -1.5$ in all cases. We indicate a slope of -1.5 in Figure C2 with a dotted black line. Thus, while the hydro simulations do not produce halos with central slopes $\alpha(r_{\rm fid}) \sim 0$, most of the sample is still more cored than the corresponding DMO case. Moreover, $r_{\rm fid}$ is well outside the dark matter core size. Only the most quickly rising systems have slopes slightly higher than the DMO runs, likely because of the presence of a dense stellar component driving adiabatic contraction (G. R. Blumenthal et al. 1986; A. A. Dutton et al. 2005; O. Y. Gnedin et al. 2011).

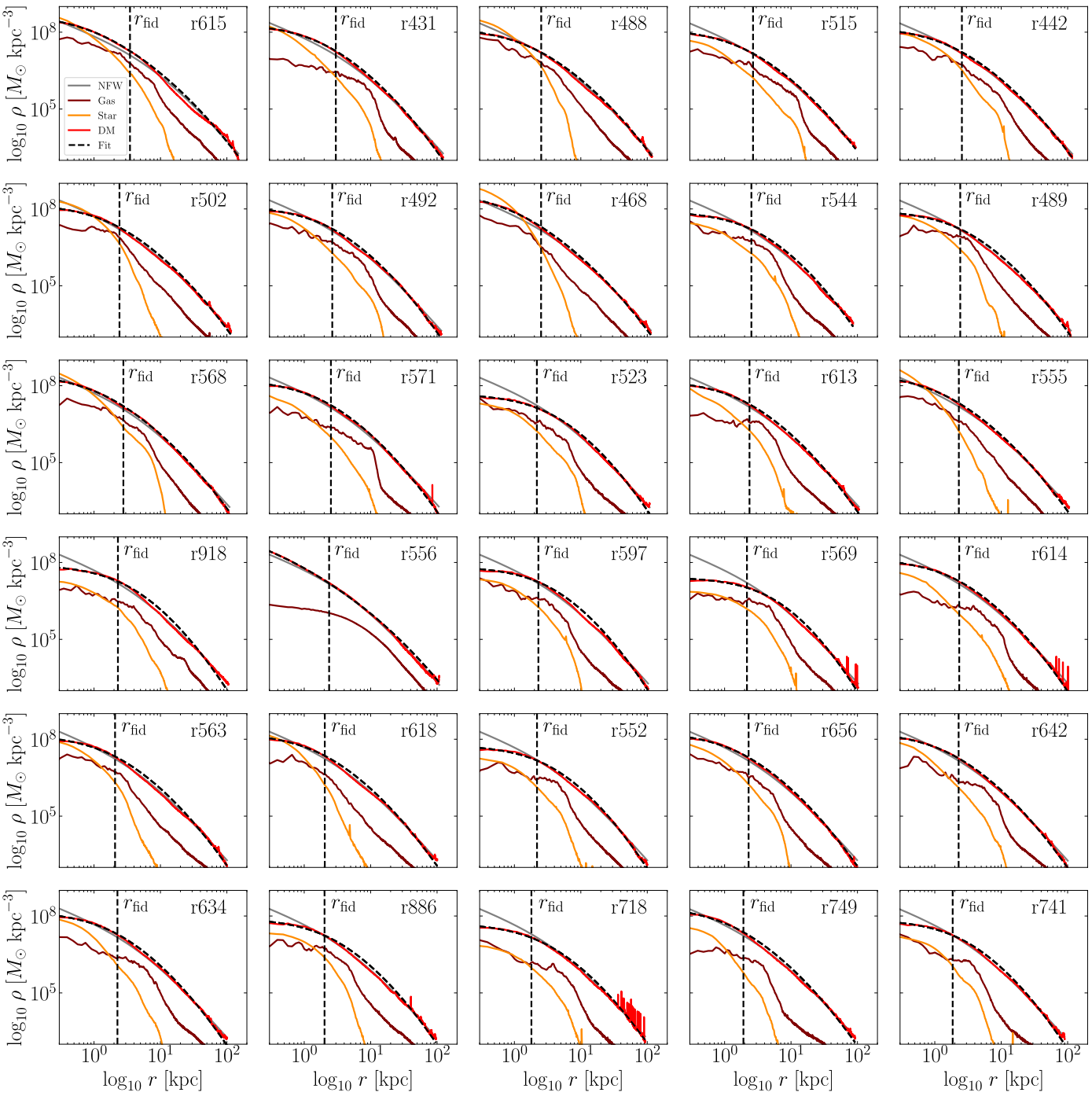


Figure C1. Density profiles for the 30 most-massive Massive Dwarf zooms are shown in maroon for gas, orange for stars, and red for dark matter. Cored Einasto fits are shown in the black dashed lines and the NFW in gray. The dashed black vertical line in each subpanel indicates $r_{\rm fid}$, the point where we measure the density slope α.

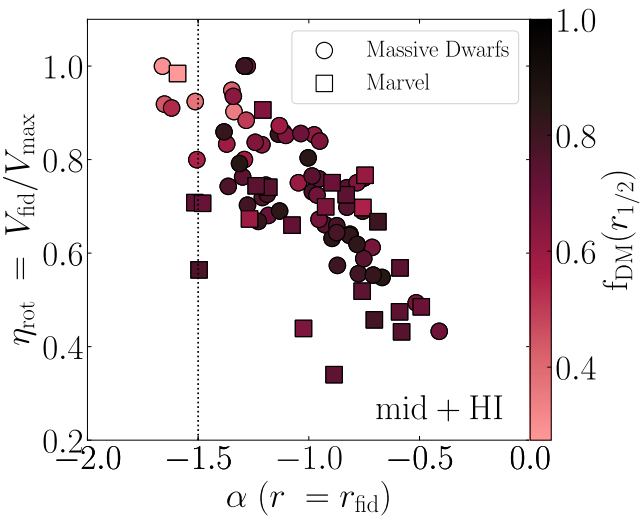


Figure C2. $\eta_{\rm rot}$ versus inner slope α colored by the dark matter mass fraction within $r_{1/2}$, $f_{\rm DM}(r_{1/2})$, for the Massive Dwarf (circles) and Marvel (squares) galaxies at $z = 0$. The black dotted line at $\alpha = -1.5$ represents the DMO prediction. The inner slope α is measured at $r_{\rm fid}$. More quickly (slowly) rising RCs have steeper (shallower) dark matter slopes.

ORCID iDs

Akaxia Cruz https://orcid.org/0000-0001-7831-4892
Alyson M. Brooks https://orcid.org/0000-0002-0372-3736
Mariangela Lisanti https://orcid.org/0000-0002-8495-8659
Annika H. G. Peter https://orcid.org/0000-0002-8040-6785
Robel Geda https://orcid.org/0000-0003-1509-9966
Thomas Quinn https://orcid.org/0000-0001-5510-2803
Michael Tremmel https://orcid.org/0000-0002-4353-0306
Ferah Munshi https://orcid.org/0000-0002-9581-0297
Ben Keller https://orcid.org/0000-0002-9642-7193
James Wadsley https://orcid.org/0000-0001-8745-0263

References

Arnett, D. 1996, Supernovae and Nucleosynthesis: An Investigation of the History of Matter, from the Big Bang to the Present (Princeton Univ. Press)
Azartash-Namin, B., Engelhardt, A., Munshi, F., et al. 2024, ApJ, 970, 40
Bellovary, J. M., Cleary, C. E., Munshi, F., et al. 2019, MNRAS, 482, 2913
Benavides, J. A., Sales, L. V., Wetzel, A., et al. 2025, MNRAS, 544, 4651
Benítez-Llambay, A., Frenk, C. S., Ludlow, A. D., & Navarro, J. F. 2019, MNRAS, 488, 2387
Binney, J., & Tremaine, S. 2008, Galactic Dynamics: Second Edition (Princeton Univ. Press)
Blumenthal, G. R., Faber, S. M., Flores, R., & Primack, J. R. 1986, ApJ, 301, 27
Booth, C. M., & Schaye, J. 2009, MNRAS, 398, 53
Bosma, A. 1981, AJ, 86, 1825
Bovy, J. 2026, Dynamics and Astrophysics of Galaxies (Princeton Univ. Press)
Bradford, J. D., Geha, M. C., & van den Bosch, F. C. 2016, ApJ, 832, 11
Broeils, A. H., & Rhee, M. H. 1997, A&A, 324, 877
Brook, C. B. 2015, MNRAS, 454, 1719
Brook, C. B., Governato, F., Roškar, R., et al. 2011, MNRAS, 415, 1051
Campbell, D. J. R., Frenk, C. S., Jenkins, A., et al. 2017, MNRAS, 469, 2335
Carlsten, S. G., Greene, J. E., Greco, J. P., Beaton, R. L., & Kado-Fong, E. 2021, ApJ, 922, 267
Catinella, B., Giovanelli, R., & Haynes, M. P. 2006, ApJ, 640, 751
Celiz, B. M., Navarro, J. F., Abadi, M. G., & Springel, V. 2025, A&A, 699, A12
Christensen, C., Quinn, T., Governato, F., et al. 2012, MNRAS, 425, 3058
Christensen, C. R., Brooks, A. M., Munshi, F., et al. 2024, ApJ, 961, 236
Christensen, C. R., Governato, F., Quinn, T., et al. 2014, MNRAS, 440, 2843
Collins, M. L. M., & Read, J. I. 2022, NatAs, 6, 647
Crain, R. A., Schaye, J., Bower, R. G., et al. 2015, MNRAS, 450, 1937
Dalcanton, J. J., & Stilp, A. M. 2010, ApJ, 721, 547
de Blok, W. J. G. 2010, AdAst, 2010, 789293
de Blok, W. J. G., McGaugh, S. S., Bosma, A., & Rubin, V. C. 2001, ApJL, 552, L23
Del Popolo, A., Le Delliou, M., & Lee, X. 2018, Galax, 6, 67
Di Cintio, A., Brook, C. B., Dutton, A. A., et al. 2014a, MNRAS, 441, 2986
Di Cintio, A., Brook, C. B., Macciò, A. V., et al. 2014b, MNRAS, 437, 415
Downing, E. R., & Oman, K. A. 2023, MNRAS, 522, 3318
Dubois, Y., Beckmann, R., Bournaud, F., et al. 2021, A&A, 651, A109
Dutton, A. A., Buck, T., Macciò, A. V., et al. 2020, MNRAS, 499, 2648
Dutton, A. A., Courteau, S., de Jong, R., & Carignan, C. 2005, ApJ, 619, 218
Dutton, A. A., Macciò, A. V., Buck, T., et al. 2019, MNRAS, 486, 655
El-Badry, K., Quataert, E., Wetzel, A., et al. 2018, MNRAS, 473, 1930
El-Badry, K., Wetzel, A. R., Geha, M., et al. 2017, ApJ, 835, 193
Flores, R. A., & Primack, J. R. 1994, ApJL, 427, L1
Frank, B. S., de Blok, W. J. G., Walter, F., Leroy, A., & Carignan, C. 2016, AJ, 151, 94
Frosst, M., Courteau, S., Arora, N., et al. 2022, MNRAS, 514, 3510
Geda, R., Crawford, S. M., Hunt, L., et al. 2022, AJ, 163, 202
Geda, R., Cruz, A., Wright, A. C., et al. 2026, ApJ, 1004, 110
Genel, S., Bryan, G. L., Springel, V., et al. 2019, ApJ, 871, 21
Gnedin, O. Y., Ceverino, D., Gnedin, N. Y., et al. 2011, arXiv:1108.5736
Governato, F., Brook, C., Mayer, L., et al. 2010, Natur, 463, 203
Governato, F., Zolotov, A., Pontzen, A., et al. 2012, MNRAS, 422, 1231
Graus, A. S., Bullock, J. S., Fitts, A., et al. 2019, MNRAS, 490, 1186
Haardt, F., & Madau, P. 2012, ApJ, 746, 125
Hopkins, P. F., Wetzel, A., Kereš, D., et al. 2018, MNRAS, 480, 800
Jackson, R. A., Navarro, J. F., Santos-Santos, I. M. E., et al. 2025, MNRAS, 539, 3797
Jahn, E. D., Sales, L. V., Marinacci, F., et al. 2023, MNRAS, 520, 461
Jiang, F., Dekel, A., Freundlich, J., et al. 2019, MNRAS, 487, 5272
Kaplinghat, M., Keeley, R. E., Linden, T., & Yu, H.-B. 2014, PhRvL, 113, 021302
Kaplinghat, M., Ren, T., & Yu, H.-B. 2020, JCAP, 2020, 027
Keith, B., Munshi, F., Brooks, A. M., et al. 2025, ApJ, 986, 138
Keller, B. W., Wadsley, J., Benincasa, S. M., & Couchman, H. M. P. 2014, MNRAS, 442, 3013
Keller, B. W., Wadsley, J. W., Wang, L., & Kruijssen, J. M. D. 2019, MNRAS, 482, 2244
Klein, C., Bullock, J. S., Moreno, J., et al. 2024, MNRAS, 532, 538
Knollmann, S. R., & Knebe, A. 2009, ApJS, 182, 608
Krause, M. G. H., Offner, S. S. R., Charbonnel, C., et al. 2020, SSRv, 216, 64
Kroupa, P. 2001, MNRAS, 322, 231
Kuzio de Naray, R., McGaugh, S. S., de Blok, W. J. G., & Bosma, A. 2006, ApJS, 165, 461
Lazar, A., Bullock, J. S., Boylan-Kolchin, M., et al. 2020, MNRAS, 497, 2393
Lelli, F., McGaugh, S. S., & Schombert, J. M. 2016a, AJ, 152, 157
Lelli, F., McGaugh, S. S., & Schombert, J. M. 2016b, ApJL, 816, L14
Lelli, F., Verheijen, M., Fraternali, F., & Sancisi, R. 2012, A&A, 544, A145
Ludlow, A. D., Bose, S., Angulo, R. E., et al. 2016, MNRAS, 460, 1214
Ludlow, A. D., Schaye, J., & Bower, R. 2019a, MNRAS, 488, 3663
Ludlow, A. D., Schaye, J., Schaller, M., & Richings, J. 2019b, MNRAS, 488, L123
Lupi, A., Volonteri, M., & Silk, J. 2017, MNRAS, 470, 1673
Mancera Piña, P. E., Fraternali, F., Oosterloo, T., et al. 2022, MNRAS, 514, 3329
Marasco, A., Oman, K. A., Navarro, J. F., Frenk, C. S., & Oosterloo, T. 2018, MNRAS, 476, 2168
Marigo, P., Girardi, L., Bressan, A., et al. 2008, A&A, 482, 883
Mashchenko, S., Wadsley, J., & Couchman, H. M. P. 2008, Sci, 319, 174
McGaugh, S. S., & Schombert, J. M. 2014, AJ, 148, 77
McQuinn, K. B. W., Adams, E. A. K., Cannon, J. M., et al. 2022, ApJ, 940, 8
Menon, H., Wesolowski, L., Zheng, G., et al. 2015, ComAC, 2, 1
Mina, M., Shen, S., Keller, B. W., et al. 2021, A&A, 655, A22
Moore, B. 1994, Natur, 370, 629
Munshi, F., Brooks, A. M., Applebaum, E., et al. 2021, ApJ, 923, 35
Navarro, J. F., Frenk, C. S., & White, S. D. M. 1996, ApJ, 462, 563
Navarro, J. F., Frenk, C. S., & White, S. D. M. 1997, ApJ, 490, 493
Oh, S.-H., de Blok, W. J. G., Brinks, E., Walter, F., & Kennicutt, R. C. J. 2011, AJ, 141, 193
Oman, K. A., Marasco, A., Navarro, J. F., et al. 2019, MNRAS, 482, 821
Oman, K. A., Navarro, J. F., Fattahi, A., et al. 2015, MNRAS, 452, 3650
Petrosian, V. 1976, ApJL, 210, L53
Pfalzner, S., Kaczmarek, T., & Olczak, C. 2012, A&A, 545, A122
Piacitelli, D. R., Brooks, A. M., Christensen, C., et al. 2025, ApJ, 993, 230
Pillepich, A., Nelson, D., Springel, V., et al. 2019, MNRAS, 490, 3196

Pineda, J. C. B., Hayward, C. C., Springel, V., & Mendes de Oliveira, C. 2017, MNRAS, 466, 63
Planck Collaboration, Ade, P. A. R., Aghanim, N., et al. 2014, A&A, 571, A16
Planck Collaboration, Aghanim, N., Akrami, Y., et al. 2020, A&A, 641, A6
Pontzen, A., & Governato, F. 2012, MNRAS, 421, 3464
Pontzen, A., Governato, F., Pettini, M., et al. 2008, MNRAS, 390, 1349
Pontzen, A., Roškar, R., Stinson, G. S., & Woods, R. 2013, pynbody: N-Body/SPH analysis for python, Astrophysics Source Code Library, ascl:1305.002
Power, C., Navarro, J. F., Jenkins, A., et al. 2003, MNRAS, 338, 14
Read, J. I., Agertz, O., & Collins, M. L. M. 2016a, MNRAS, 459, 2573
Read, J. I., & Gilmore, G. 2005, MNRAS, 356, 107
Read, J. I., Iorio, G., Agertz, O., & Fraternali, F. 2016b, MNRAS, 462, 3628
Regan, J. 2023, OJAp, 6, 12
Regan, J. A., Wise, J. H., Woods, T. E., et al. 2020, OJAp, 3, 15
Relatores, N. C., Newman, A. B., Simon, J. D., et al. 2019a, ApJ, 873, 5
Relatores, N. C., Newman, A. B., Simon, J. D., et al. 2019b, ApJ, 887, 94
Ren, T., Kwa, A., Kaplinghat, M., & Yu, H.-B. 2019, PhRvX, 9, 031020
Riggs, C. L., Brooks, A. M., Munshi, F., et al. 2024, ApJ, 977, 20
Roper, F. A., Oman, K. A., Frenk, C. S., et al. 2023, MNRAS, 521, 1316
Ruan, D., Brooks, A. M., Cruz, A., et al. 2025, MNRAS, 541, 2180
Rubin, V. C., Ford, W. K. J., & Thonnard, N. 1980, ApJ, 238, 471
Sales, L. V., Navarro, J. F., Oman, K., et al. 2017, MNRAS, 464, 2419
Sales, L. V., Wetzel, A., & Fattahi, A. 2022, NatAs, 6, 897
Sands, I. S., Hopkins, P. F., Shen, X., et al. 2026, ApJ, 1000, 127
Santos-Santos, I. M., Di Cintio, A., Brook, C. B., et al. 2018, MNRAS, 473, 4392
Santos-Santos, I. M. E., Navarro, J. F., Robertson, A., et al. 2020, MNRAS, 495, 58
Schaye, J., Crain, R. A., Bower, R. G., et al. 2015, MNRAS, 446, 521
Sérsic, J. L. 1963, BAAA, 6, 41
Simon, J. D., Bolatto, A. D., Leroy, A., & Blitz, L. 2003, ApJ, 596, 957
Spergel, D. N., Bean, R., Doré, O., et al. 2007, ApJS, 170, 377
Spergel, D. N., & Steinhardt, P. J. 2000, PhRvL, 84, 3760
Springel, V., Frenk, C. S., & White, S. D. M. 2006, Natur, 440, 1137
Stinson, G., Seth, A., Katz, N., et al. 2006, MNRAS, 373, 1074
Stinson, G. S., Brook, C., Macciò, A. V., et al. 2013, MNRAS, 428, 129
Strauss, M. A., Weinberg, D. H., Lupton, R. H., et al. 2002, AJ, 124, 1810
Teyssier, R., Pontzen, A., Dubois, Y., & Read, J. I. 2013, MNRAS, 429, 3068
Tollet, E., Macciò, A. V., Dutton, A. A., et al. 2016, MNRAS, 456, 3542
Tremmel, M., Governato, F., Volonteri, M., & Quinn, T. R. 2015, MNRAS, 451, 1868
Tremmel, M., Governato, F., Volonteri, M., Quinn, T. R., & Pontzen, A. 2018, MNRAS, 475, 4967
Tremmel, M., Karcher, M., Governato, F., et al. 2017, MNRAS, 470, 1121
Valenzuela, O., Rhee, G., Klypin, A., et al. 2007, ApJ, 657, 773
van der Wel, A., Straughn, A. N., Rix, H. W., et al. 2011, ApJ, 742, 111
Verbeke, R., Papastergis, E., Ponomareva, A. A., Rathi, S., & De Rijcke, S. 2017, A&A, 607, A13
Wadsley, J. W., Keller, B. W., & Quinn, T. R. 2017, MNRAS, 471, 2357
Wadsley, J. W., Stadel, J., & Quinn, T. 2004, NewA, 9, 137
Wang, J., Koribalski, B. S., Serra, P., et al. 2016, MNRAS, 460, 2143
Wang, L., Dutton, A. A., Stinson, G. S., et al. 2015, MNRAS, 454, 83
Williams, L. L. R., Hjorth, J., & Skillman, E. D. 2025, JCAP, 2025, 052
Wise, J. H., Regan, J. A., O'Shea, B. W., et al. 2019, Natur, 566, 85
Zentner, A., Dandavate, S., Slone, O., & Lisanti, M. 2022, JCAP, 2022, 031